

A Computational Model for Flexoelectricity-Driven Contact Electrification

Han Hu^a, Xiaoying Zhuang^{a,b,*}, Timon Rabczuk^c

^a*Institute of Photonics, Faculty of Mathematics and Physics, Leibniz University Hannover, Hannover, 30167, Germany*

^b*College of Civil Engineering, Department of Geotechnical Engineering, Tongji University, Shanghai, 200092, China*

^c*Institute of Structural Mechanics, Bauhaus University Weimar, 99423 Weimar, Germany*

Abstract

Recent theoretical studies show that nanoscale contact on dielectric substrates can induce flexoelectric polarization large enough to drive electron transfer. This has been supported by experimental evidence, indicating that contact electrification is inherently a coupled electromechanical phenomenon. In this work, we develop a computational model for flexoelectricity-driven contact electrification that integrates finite-deformation flexoelectricity with contact mechanics and physically motivated charge transfer. A tunneling transparency function is introduced to regulate the interfacial channel based on the WKB approximation, capturing the irreversible charge trapping during unloading. Three contact scenarios are investigated with specific hypotheses for charge transfer: unbiased metal-dielectric contact driven by surface polarization, biased contact restricted to carriers of a single polarity, and dielectric-dielectric contact where surface states with finite capacity limit the transferable charge. The model is compared with atomic force microscopy measurements on PMMA and PDAP substrates under both biased and unbiased conditions. For contact between identical dielectric materials, we show that geometric asymmetry in surface curvature is sufficient to induce charge separation, with polarity reversal occurring at a critical surface wavenumber. Three-dimensional simulations on random rough surfaces reproduce the mosaic charge distributions observed experimentally, confirming that contact-induced local strain gradient heterogeneity can generate spatially non-uniform charge patterns without introducing any material inhomogeneity.

Keywords: Contact electrification, Flexoelectricity, Triboelectric nanogenerator,

*Corresponding author

Email address: zhuang@iop.uni-hannover.de (Xiaoying Zhuang)

1. Introduction

1.1. Background and motivation

Contact electrification (CE), also known as triboelectrification when accompanied by friction, occurs when surfaces become net charged after contact and separation [1, 2]. Although this phenomenon was first documented over 2,600 years ago by Thales of Miletus, who observed the electrostatic attraction of amber, it remains incompletely understood in interface science [3, 4]. CE spans a vast range of length scales, from electrostatic-induced segregation in pharmaceutical powders [5] and electrophotography [6] to high-energy macroscale phenomena such as volcanic lightning and dust storms [7, 8]. Although CE was historically considered an industrial hazard (e.g., electrostatic discharge that damages electronics or dust explosions in coal plants [9, 10, 11]), it has recently attracted renewed interest as an energy-harvesting mechanism [12, 13, 14].

Over the past decade, the invention of the triboelectric nanogenerator (TENG) has transformed CE from a nuisance into a practical energy harvesting technology [12, 13, 14]. The operating mechanism of TENGs relies on coupling contact electrification with electrostatic induction to convert mechanical energy such as random vibrations, wind, ocean waves, or human motion, into electricity [15, 16, 17, 18]. Due to their broad material selectivity, light weight structure, and cost-effectiveness, TENGs have been applied to power the Internet of Things, self-powered sensors, and wearable electronics [19, 20, 21]. Recent work has also extended TENG applications to chemical sensing, blue energy harvesting, and high-voltage power sources [22, 23, 24, 25].

However, the optimization of these devices is limited by a lack of consensus regarding the fundamental charge transfer mechanisms [25, 26]. Although triboelectric series have been developed based on empirical observations [27, 28], quantitative prediction from intrinsic material properties remains challenging. Recent theoretical works propose that large strain gradients generated at contacting asperities induce sufficiently high levels of flexoelectric polarization to bend interfacial energy bands and drive electron tunneling [29, 30, 31]. This mechanism has been experimentally validated by Lin et al. [32] and Qiao et al. [33], who demonstrated that altering the contact force and consequently the local strain gradient can manipulate the

magnitude and even reverse the polarity of charge transfer. These findings suggest that CE is fundamentally a coupled electromechanical phenomenon. Therefore, a rigorous computational approach is needed to quantify the thermodynamic drive provided by the interface’s mechanical state [34].

1.2. Literature Review

1.2.1. Classical Mechanisms of Contact Electrification

The physical origin of charge transfer in CE has been debated for over a century. Hypotheses can be historically categorized into three primary mechanisms: electron transfer, ion transfer, and material transfer [1, 35]. The electron transfer model suggests that thermodynamic equilibrium drives electrons from a material with a higher Fermi level to one with a lower Fermi level until electrochemical potentials equalize [3]. This model is well-accepted for metal-metal and metal-semiconductor contacts [36, 37]. For insulators, the surface state theory extends this framework by postulating that localized electronic states exist within the forbidden bandgap at the material surface, arising from lattice termination or surface defects [3, 4]. These states define an effective Fermi level, enabling electron tunneling between contacting surfaces in a manner analogous to metals [38, 39]. More recently, Wang et al. proposed the “overlapped electron-cloud model”, which provides an atomistic perspective: mechanical compression brings atoms into the repulsive force regime where interatomic distances fall below the normal bonding length, causing electron clouds to overlap and lowering the potential barrier for electron transition [40, 41].

In contrast, the ion transfer model suggests that mobile ions on the surface or within aqueous adlayers are the primary charge carriers [42, 43, 44]. This mechanism is particularly relevant for polymers containing mobile ionic groups, or for contacts in high-humidity environments, where capillary water bridges facilitate ion migration [45]. For example, researchers found that the partitioning of hydroxide ions (OH^-) and protons (H^+) on surfaces drives charging in insulating polymers [46]. However, this mechanism becomes negligible under dry conditions or when materials lack mobile ions [1]. The third mechanism is material transfer, where nanoscale fragments of material are mechanically torn and transferred between contacting bodies, carrying net charge with them [47, 48]. Experimental evidence correlates the amount of transferred material with charge density [49], although material transfer can occur independently of charging [50].

While no single model captures the full complexity of CE, researchers widely recognize that electron transfer dominates in metal-dielectric and dielectric-dielectric contacts under controlled conditions, whereas ion and material transfer contribute under specific environmental or tribological conditions [1, 35, 51].

1.2.2. The Role of Flexoelectricity in CE

The classical mechanisms discussed above struggle to explain several anomalous observations, such as charge transfer between chemically identical materials and the reversal of charge polarity under varying contact pressure [52, 53, 8]. A common feature of these anomalies is their dependence on the mechanical state of the contact, suggesting that deformation itself plays a fundamental role in the charging process. Mechanical contact at nanoscale asperities generates highly non-uniform strain fields, with strain gradients scaling inversely with the radius of curvature and reaching magnitudes of 10^7 – 10^9 m^{-1} for typical asperity dimensions of 10–100 nm [29, 30]. At such magnitudes, the flexoelectric effect becomes significant. Flexoelectricity is the linear electromechanical coupling between strain gradients and electric polarization [54, 55]. Unlike piezoelectricity, which requires non-centrosymmetric crystal structures, flexoelectricity arises from the local breaking of inversion symmetry by non-uniform deformation and is therefore present in all dielectric materials regardless of their crystal class [56, 57, 58].

The flexoelectric polarization induced at contact interfaces generates a localized flexoelectric potential difference, which can reach magnitudes of 1–10 V [29, 31]. This potential difference bends the electronic energy bands relative to the Fermi level, and when the band bending exceeds the intrinsic work function difference, it can reverse the thermodynamic drive for electron transfer, providing a natural explanation for pressure-dependent polarity reversal and size-dependent charging in granular systems [59, 60]. Theoretical frameworks by Mizzi et al.[29] and Persson[30] first quantified this mechanism, showing that the flexoelectric field at nanoscale asperity contacts is sufficient to drive charge separation. This mechanism was subsequently validated by atomic force microscopy experiments. For instance, Qiao et al.[33] and Lin et al.[32] independently demonstrated that varying the contact force can induce energy band bending and reverse the polarity of charge transfer between a tip and various substrates. Building upon these experimental insights, Olson and Marks developed quantitative models that incorporate flexoelectric band bending and electron tunneling kinetics [31, 34, 61].

Collectively, these findings establish that contact electrification is fundamentally a coupled electromechanical phenomenon.

1.2.3. Computational Modeling of Flexoelectricity

The recognition of CE as a coupled electromechanical phenomenon necessitates computational frameworks capable of resolving the significant strain gradients at nanoscale contacts and their associated flexoelectric responses. Modeling flexoelectricity presents unique mathematical challenges because the presence of strain gradient terms yields fourth-order partial differential equations (PDEs) for the displacement field [62, 63]. In weak form, these equations contain second-order derivatives, requiring basis functions with C^1 -continuity across element boundaries [64].

To address this continuity requirement, three principal numerical strategies have emerged [64]. Mixed finite element method (MFEM) treats displacement gradients as independent degrees of freedom, enforcing the kinematic constraint through Lagrange multipliers or penalty terms, thereby reducing the problem to one solvable with standard C^0 elements [65, 66]. While compatible with existing finite element architectures, this approach significantly increases the degrees of freedom. Meshfree methods construct inherently smooth shape functions that naturally accommodate higher-order derivatives, excelling in handling large deformations though at greater computational expense [67, 68]. Isogeometric analysis (IGA), which uses Non-Uniform Rational B-Splines (NURBS) as basis functions, is now widely adopted for flexoelectric modeling [69, 70]. By construction, NURBS provide C^{p-1} continuity for degree- p splines, naturally satisfying the C^1 requirement without auxiliary variables, while maintaining exact geometric representation [64]. These numerical tools have enabled investigations spanning topology optimization, soft dielectrics at finite deformations, semiconductor devices, and architected metamaterials [71, 72, 73, 74, 75, 76, 77].

While computational flexoelectricity is well established, its application to contact electrification modeling is relatively recent. Silavnieks et al. [78] developed a flexoelectricity-driven contact-separation model using asymptotic analytical solutions for Hertzian sphere-on-flat contacts, demonstrating that accounting for unloading processes significantly affects residual charge predictions as charge backflow occurs while interfacial gaps remain below tunneling cutoff distances. Similarly, Olson and Marks [50] proposed a quantitative model successfully incorporating semiconductor depletion layers and flexoelectric polarization for metal-

semiconductor systems. These studies represent the first steps toward integrating flexoelectric theory with contact mechanics for CE prediction.

Building upon these foundations, several opportunities for further development motivate the present work. To begin with, extending from analytical mechanics to fully coupled numerical frameworks, enriched with nanoscale Van der Waals adhesion, enables the resolution of flexoelectric coupling and contact behavior under finite deformation. Furthermore, the transition from equilibrium polarization-induced charge demand during loading to frozen residual charge after separation requires phenomenological rules informed by quantum tunneling physics to be incorporated into continuum frameworks. Additionally, since experimental measurements invariably capture only the final residual charge of the sample surfaces, the computational framework must resolve the charge redistribution that occurs as the contact area shrinks and tunneling channels close. Finally, numerical frameworks naturally accommodate complex geometries, such as the surface roughness ubiquitous in realistic contact scenarios, allowing for the investigation of geometry-induced charge patterns.

1.3. Contributions of the present work

The present work addresses these gaps by developing a computational model for flexoelectricity-driven contact electrification. At the core of this model, a tunneling transparency function inspired by the WKB approximation is proposed to govern charge transfer across the nanoscale interface gap. Based on this framework, specific charge transfer hypotheses are formulated for three contact configurations. In unbiased metal-dielectric contact, the surface polarization charge induced by flexoelectricity drives electron transfer from the conducting tip; in biased contact, the externally applied field acts as a selective reservoir, restricting charge transfer to carriers of a single sign; and in dielectric-dielectric contact, surface states with finite capacity serve as the charge reservoir, allowing charge separation even between identical materials. To evaluate the model's physical fidelity, the framework is qualitatively compared with atomic force microscopy measurements. It is subsequently applied to rough-surface contacts, where it successfully reproduces several experimentally observed phenomena. These include curvature-dependent charge separation, polarity reversal controlled by surface waviness, and spatially heterogeneous mosaic charge patterns, offering mechanistic explanations grounded in contact-induced local strain gradient variations.

1.4. Organization of the paper

The remainder of this paper is organized as follows: Section 2 establishes the theoretical framework, covering finite-deformation flexoelectricity, contact mechanics with adhesion, and the specific charge transfer rules for the three contact scenarios. Building upon this formulation, Section 3 compares the model predictions with AFM experiments on metal-dielectric contacts under both unbiased and biased conditions, supplemented by parametric studies on tip radius and tunneling length. The framework is subsequently applied in Section 4 to investigate dielectric-dielectric contact between identical materials, exploring geometry-induced charge separation on two-dimensional wavy surfaces and three-dimensional random rough profiles. Finally, Section 5 critically discusses the model's limitations and relates our approach to existing literature, before concluding remarks and future directions are summarized in Section 6.

2. Theoretical Framework

This section presents the theoretical foundations of the computational framework for flexoelectricity-driven contact electrification. We begin with finite-deformation flexoelectricity, then describe the contact mechanics constraints, and finally detail the charge-transfer mechanisms for different contact scenarios.

2.1. Finite deformation flexoelectricity

Consider a dielectric body occupying the domain $\mathcal{B}_0 \subset \mathbb{R}^3$ in the reference configuration, with boundary $\partial\mathcal{B}_0$. The deformation is described by the mapping $\boldsymbol{\chi} : \mathcal{B}_0 \rightarrow \mathcal{B}_t$, where \mathcal{B}_t denotes the current configuration. The displacement field is $\mathbf{u} = \boldsymbol{\chi} - \mathbf{X}$, where \mathbf{X} represents the material coordinates. The deformation gradient is defined as $\mathbf{F} = \partial\boldsymbol{\chi}/\partial\mathbf{X}$, with the Jacobian determinant $J = \det(\mathbf{F})$. The right Cauchy–Green deformation tensor is $\mathbf{C} = \mathbf{F}^T\mathbf{F}$, and the Green–Lagrange strain tensor is

$$\boldsymbol{\mathcal{E}} = \frac{1}{2}(\mathbf{C} - \mathbf{I}), \quad (1)$$

where \mathbf{I} is the identity tensor. The strain gradient tensor is defined as $\boldsymbol{\mathcal{G}} = \partial\boldsymbol{\mathcal{E}}/\partial\mathbf{X}$.

The Lagrangian electric field is $\mathbf{E} = -\partial\Phi/\partial\mathbf{X}$, where Φ denotes the electric potential. We formulate the electromechanical coupled response within a variational framework characterized

by the electric Gibbs free energy density per unit reference volume:

$$\bar{\Psi}^{\text{Gib}}(\boldsymbol{\mathcal{E}}, \boldsymbol{\mathcal{G}}, \boldsymbol{E}) = \bar{\Psi}^{\text{Mech}}(\boldsymbol{\mathcal{E}}, \boldsymbol{\mathcal{G}}) + \bar{\Psi}^{\text{Diele}}(\boldsymbol{\mathcal{E}}, \boldsymbol{E}) + \bar{\Psi}^{\text{Flexo}}(\boldsymbol{\mathcal{E}}, \boldsymbol{\mathcal{G}}, \boldsymbol{E}) - \bar{\Psi}^{\text{Elec}}(\boldsymbol{\mathcal{E}}, \boldsymbol{E}), \quad (2)$$

with the individual contributions defined as [79]:

$$\bar{\Psi}^{\text{Mech}}(\boldsymbol{\mathcal{E}}, \boldsymbol{\mathcal{G}}) = \bar{\Psi}^{\text{Elast}}(\boldsymbol{\mathcal{E}}) + \frac{1}{2} \boldsymbol{\mathcal{G}} : \bar{\boldsymbol{h}} : \boldsymbol{\mathcal{G}}, \quad (3)$$

$$\bar{\Psi}^{\text{Diele}}(\boldsymbol{\mathcal{E}}, \boldsymbol{E}) = -\frac{J}{2} (\epsilon - \epsilon_0) \boldsymbol{E} \cdot \boldsymbol{C}^{-1} \cdot \boldsymbol{E}, \quad (4)$$

$$\bar{\Psi}^{\text{Flexo}}(\boldsymbol{\mathcal{E}}, \boldsymbol{\mathcal{G}}, \boldsymbol{E}) = -J \boldsymbol{E} \cdot \boldsymbol{C}^{-1} \cdot \boldsymbol{\mu} : \boldsymbol{\mathcal{G}}, \quad (5)$$

$$\bar{\Psi}^{\text{Elec}}(\boldsymbol{\mathcal{E}}, \boldsymbol{E}) = \frac{J \epsilon_0}{2} \boldsymbol{E} \cdot \boldsymbol{C}^{-1} \cdot \boldsymbol{E}, \quad (6)$$

where $\bar{\Psi}^{\text{Elast}}$ is the hyperelastic strain energy density (we adopt the neo-Hookean model), $\bar{\boldsymbol{h}}$ is a sixth-order strain gradient elasticity tensor, $\boldsymbol{\mu}$ is the fourth-order flexoelectric coefficient tensor, ϵ_0 is the vacuum permittivity, and ϵ is the material permittivity.

The constitutive relations are derived from the Gibbs free energy density. The second Piola–Kirchhoff stress tensor is

$$\boldsymbol{S} := \frac{\partial \bar{\Psi}^{\text{Mech}}}{\partial \boldsymbol{\mathcal{E}}}, \quad (7)$$

and the second Piola–Kirchhoff double stress tensor is

$$\boldsymbol{\Sigma} := \frac{\partial \bar{\Psi}^{\text{Gib}}}{\partial \boldsymbol{\mathcal{G}}} = \bar{\boldsymbol{h}} : \boldsymbol{\mathcal{G}} - J \boldsymbol{E} \cdot \boldsymbol{C}^{-1} \cdot \boldsymbol{\mu}. \quad (8)$$

The Lagrangian electric displacement is

$$\boldsymbol{D} = -\frac{\partial \bar{\Psi}^{\text{Gib}}}{\partial \boldsymbol{E}} = J \boldsymbol{C}^{-1} \cdot \left(\epsilon \boldsymbol{E} + \boldsymbol{\mu} : \boldsymbol{\mathcal{G}} \right). \quad (9)$$

In Eqs. (4)–(9), the $J \boldsymbol{C}^{-1}$ mapping terms account for the transformation of strictly spatial electrostatic definitions into the reference configuration. The second term in Eq. (9) represents the flexoelectric contribution to the electric displacement, which couples the strain gradient to the electric response. The Maxwell stress tensor, which accounts for electrostatic body forces

in the reference configuration, is given by the second Piola–Maxwell stress form [76]

$$\mathbf{S}^{\text{MW}} = (\mathbf{C}^{-1} \mathbf{E}) \otimes \tilde{\mathbf{D}} - \frac{1}{2} (\mathbf{E} \cdot \tilde{\mathbf{D}}) \mathbf{C}^{-1}, \quad (10)$$

where $\tilde{\mathbf{D}} = J\mathbf{C}^{-1} \cdot \left[\epsilon \mathbf{E} + 2\boldsymbol{\mu} : \boldsymbol{\mathcal{G}} \right]$ is the auxiliary electric displacement [76].

The governing equations in the reference configuration are:

$$\nabla \cdot [\mathbf{F} (\mathbf{S} - \nabla \cdot \boldsymbol{\Sigma} + \mathbf{S}^{\text{MW}})] + \mathbf{b}_0 = \mathbf{0} \quad \text{in } \mathcal{B}_0, \quad (11)$$

$$\nabla \cdot \mathbf{D} = Q_0 \quad \text{in } \mathcal{B}_0, \quad (12)$$

where \mathbf{b}_0 is the body force per unit reference volume and Q_0 is the body charge density per unit reference volume.

The boundary conditions for the mechanical field consist of prescribed displacements $\bar{\mathbf{u}}$ on the Dirichlet boundary $\partial\mathcal{B}_0^u$, prescribed tractions $\bar{\mathbf{t}}$ on the Neumann boundary $\partial\mathcal{B}_0^t$, and prescribed higher-order tractions $\bar{\mathbf{r}}$ on the higher-order Neumann boundary $\partial\mathcal{B}_0^r$:

$$\mathbf{u} = \bar{\mathbf{u}} \quad \text{on } \partial\mathcal{B}_0^u, \quad (13)$$

$$\mathbf{F}(\mathbf{S} - \nabla \cdot \boldsymbol{\Sigma} + \mathbf{S}^{\text{MW}}) \cdot \mathbf{N} + \tilde{\mathbf{T}}^t = \bar{\mathbf{t}} \quad \text{on } \partial\mathcal{B}_0^t, \quad (14)$$

$$\tilde{\mathbf{T}}^n = \bar{\mathbf{r}} \quad \text{on } \partial\mathcal{B}_0^r, \quad (15)$$

where \mathbf{N} is the outward unit normal in the reference configuration. The terms $\tilde{\mathbf{T}}^t$ and $\tilde{\mathbf{T}}^n$ emerge from the surface divergence theorem by splitting the variation of the deformation gradient into surface-tangential and surface-normal components. The detailed index notations for $\tilde{\mathbf{T}}^t$ and $\tilde{\mathbf{T}}^n$ are provided in Appendix A. For the electrical field, the boundary conditions comprise prescribed potential $\bar{\Phi}$ on the Dirichlet boundary $\partial\mathcal{B}_0^\Phi$ and prescribed surface charge density \bar{W} on the Neumann boundary $\partial\mathcal{B}_0^W$:

$$\Phi = \bar{\Phi} \quad \text{on } \partial\mathcal{B}_0^\Phi, \quad (16)$$

$$\mathbf{D} \cdot \mathbf{N} = \bar{W} \quad \text{on } \partial\mathcal{B}_0^W. \quad (17)$$

2.2. Contact mechanics formulation

We consider a contact problem between two bodies: a “slave” body \mathcal{B}_s and a “master” body \mathcal{B}_m . The contact surface is denoted by $\partial\mathcal{B}^C$. For a point $\boldsymbol{\chi}^s$ on the slave surface, its projection onto the master surface is $\bar{\boldsymbol{\chi}}^m$, determined by minimizing the distance function. The normal gap is defined as

$$g_N = (\boldsymbol{\chi}^s - \bar{\boldsymbol{\chi}}^m) \cdot \mathbf{n}, \quad (18)$$

where \mathbf{n} is the outward unit normal of the master surface in the current configuration at the projection point.

For frictionless contact, the normal non-penetration constraints are formulated via the standard Karush–Kuhn–Tucker (KKT) conditions:

$$g_N \geq 0, \quad t_N \leq 0, \quad g_N t_N = 0 \quad \text{on } \partial\mathcal{B}_t^C, \quad (19)$$

where t_N is the normal contact traction, representing a strictly repulsive pressure in this notation.

To capture the adhesive forces that influence nanoscale contact behavior, we incorporate an exponential cohesive zone model following the formulation of Xu and Needleman [80] as modified by van den Bosch et al. [81]. This model expresses the normal traction in terms of the normal separation while naturally satisfying the requirement of vanishing traction at complete separation. For the frictionless contact considered in this work, the normal cohesive traction takes the form [82]:

$$t_N^{\text{adh}} = \frac{\phi_N}{(g_N^{\text{max}})^2} g_N \exp\left(-\frac{g_N}{g_N^{\text{max}}}\right) \quad \text{for } g_N > 0, \quad (20)$$

where a positive t_N^{adh} denotes an attractive pull between the separated surfaces. ϕ_N is the fracture energy and g_N^{max} is the characteristic length at which the cohesive traction reaches its maximum value p_N^{max} . These parameters are related through $\phi_N = e p_N^{\text{max}} g_N^{\text{max}}$, where e is Euler’s number. This formulation ensures thermodynamic consistency and provides a smooth transition from adhesive attraction to complete separation [82].

2.3. Charge transfer mechanisms

The framework postulates that interfacial charge transfer is driven by the thermodynamic force from flexoelectric surface bound charges [29, 61, 78] and is limited by tunneling kinetics [31, 83]. While the driving force and tunneling physics are universal, their manifestation differs across contact configurations depending on the nature of the contacting surfaces and the availability of charge carriers. This section develops a unified framework encompassing three contact scenarios: unbiased metal-dielectric contact, biased metal-dielectric contact, and dielectric-dielectric contact.

Before presenting the specific models, we outline the physical scenario common to all cases. Consider a contact experiment in which a probe tip is pressed against a dielectric substrate (the *loading* phase) and subsequently retracted until the two surfaces separate (the *unloading* phase). As established in Section 2.1, the deformation at the contact interface produces strain gradients, which in turn induce flexoelectric polarization in the dielectric. This polarization terminates at the surface and creates a bound charge density $\rho_b = -\nabla \cdot \mathbf{p}$ in the bulk and $\sigma_b = \mathbf{p} \cdot \mathbf{n}$ at the surface. To reach electrostatic equilibrium, free charges must be supplied to screen (compensate) this bound polarization charge [78]. The source of these free charges depends on the contact configuration: a conducting tip can supply electrons readily from the metal; when the tip is also a dielectric, surface states serve as the charge reservoir.

2.3.1. Tunneling transparency factor

Charge transfer across a nanoscale interface gap occurs primarily through quantum mechanical tunneling, where the transmission probability depends exponentially on the barrier width. According to the Wentzel–Kramers–Brillouin (WKB) approximation, the tunneling probability through a rectangular barrier of width d and height U decays exponentially as $T \sim \exp(-2\kappa d)$, where $\kappa = \sqrt{2m(U - E)}/\hbar$ is the decay constant determined by the effective electron mass m and the energy deficit below the barrier [84].

Inspired by this exponential decay, we introduce a phenomenological tunneling transparency factor $\mathcal{T} \in [0, 1]$ that smoothly interpolates between fully open ($\mathcal{T} = 1$) and fully closed ($\mathcal{T} = 0$) tunneling channels as

$$\mathcal{T} = \left[1 + \exp\left(\frac{g_N - \ell_q}{\Delta_g}\right) \right]^{-1}, \quad (21)$$

where g_N is the normal gap, ℓ_q is the characteristic tunneling length below which the channel is effectively open, and Δ_g controls the sharpness of the transition. This logistic form captures the rapid decay of transfer capability once the gap exceeds a critical distance while avoiding the numerical difficulties associated with a discontinuous step function. Based on the overlapped electron-cloud model [40, 41], we adopt $\ell_q = 0.24$ nm and $\Delta_g = 0.012$ nm in this work unless otherwise specified, corresponding to a transition zone of approximately 0.05 nm. Figure 1 illustrates the tunneling transparency factor as a function of the normal gap distance.

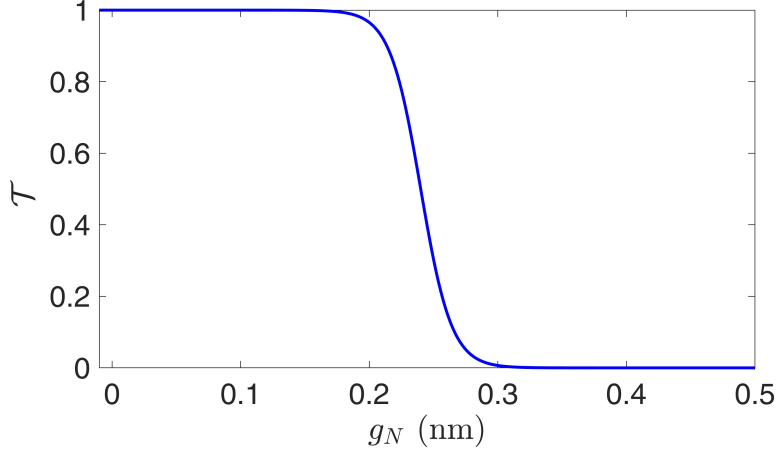


Fig. 1. Tunneling transparency factor \mathcal{T} as a function of normal gap distance g_N , with $\ell_q = 0.24$ nm and $\Delta_g = 0.012$ nm.

2.3.2. Metal-dielectric contact: Unbiased case

In this scenario, a conducting tip contacts a dielectric surface without an applied bias. The flexoelectric polarization induced by contact deformation creates bound surface charge that must be screened by free charges. The conducting tip, acting as an ideal charge reservoir, supplies these free charges through the tunneling channels described in Section 2.3.1. During loading, when the gap is closed or small and the transparency factor (Eq. (21)) is high, charge flows readily. During unloading, as the surfaces separate and gaps reopen at the contact periphery, the tunneling channels close progressively from the edge inward, “freezing” a portion of the transferred charge on the dielectric surface. To track this process, the *accumulated frozen charge* Σ_{froz} records the free charge density at each surface point throughout the loading–unloading cycle, enabling prediction of the residual charge distribution after separation.

We extract the flexoelectric polarization in the current configuration as:

$$\mathbf{p}_{\text{flexo}} = \mathbf{F}^{-\text{T}} \cdot \boldsymbol{\mu} \colon \boldsymbol{\mathcal{G}}. \quad (22)$$

This local flexoelectric polarization induces a *charge demand* $\hat{\sigma}_d$ that represents the equilibrium free charge density required to screen the bound polarization charge:

$$\hat{\sigma}_d = -\mathbf{p}_{\text{flexo}} \cdot \mathbf{n}, \quad (23)$$

with \mathbf{n} being the outward surface normal.

In the quasi-static limit, charge transfer is governed by the instantaneous equilibrium between the imposed deformation and the tunneling channel state, with no explicit time dependence. Accordingly, the actual charge transferred during any load step is determined by the increment of the equilibrium demand, regulated by the instantaneous channel transparency \mathcal{T} . This principle leads to a unified incremental update rule that applies to both loading and unloading:

$$\Sigma_{\text{froz}}^{(n)} = \Sigma_{\text{froz}}^{(n-1)} + \mathcal{T} \cdot (\hat{\sigma}_d^{(n)} - \hat{\sigma}_d^{(n-1)}). \quad (24)$$

During loading, when the tunneling channel is open ($\mathcal{T} \approx 1$), the frozen charge tracks the evolving flexoelectric demand. During unloading, as surfaces separate and the polarization demand decreases, only the incremental change can traverse the narrowing channel. Charge deposited under a wide-open channel becomes trapped as the passage closes, producing the characteristic “edge-frozen” distribution observed after complete separation. When the channel is completely closed ($\mathcal{T} = 0$), the frozen charge remains unchanged regardless of the demand evolution.

The treatment of electrical boundary conditions at the interface reflects the physics of the tunneling channel. In regions where the channel is open ($\mathcal{T} \rightarrow 1$), charge flows freely between the metal and dielectric. Numerically, this is enforced by imposing an electrical contact condition that ensures potential continuity:

$$\phi_{\text{dielectric}} = \phi_{\text{metal}} \quad \text{where } \mathcal{T} \rightarrow 1. \quad (25)$$

Under this constraint, charge transfer occurs implicitly through the coupled electromechanical solution, so that no explicit charge source term is required. In contrast, where the tunneling channel is closed ($\mathcal{T} \rightarrow 0$), the frozen charge Σ_{froz} acts as an external surface charge contributing to the electric field. The charge contribution to the electrical Neumann boundary

is:

$$\bar{\omega}^{(n)} = (1 - \mathcal{T}) \cdot \Sigma_{\text{froz}}^{(n)}, \quad (26)$$

where the factor $(1 - \mathcal{T})$ ensures a smooth transition in intermediate regions.

Figure 2 illustrates the transparency factor's role throughout the loading–unloading cycle. When the surfaces are far apart (stage a), $\mathcal{T} = 0$ and no charge can tunnel across the gap. As contact is established (stage b), tunneling channels open and free charges flow from the metal to meet the flexoelectric demand. During unloading (stage c), the gap opens first at the contact periphery, causing \mathcal{T} to decrease there while the center remains in close contact. The incremental rule permits only partial backflow through the narrowing channel, thereby yielding the irreversible “edge-frozen” charge distribution observed after complete separation (stage d).

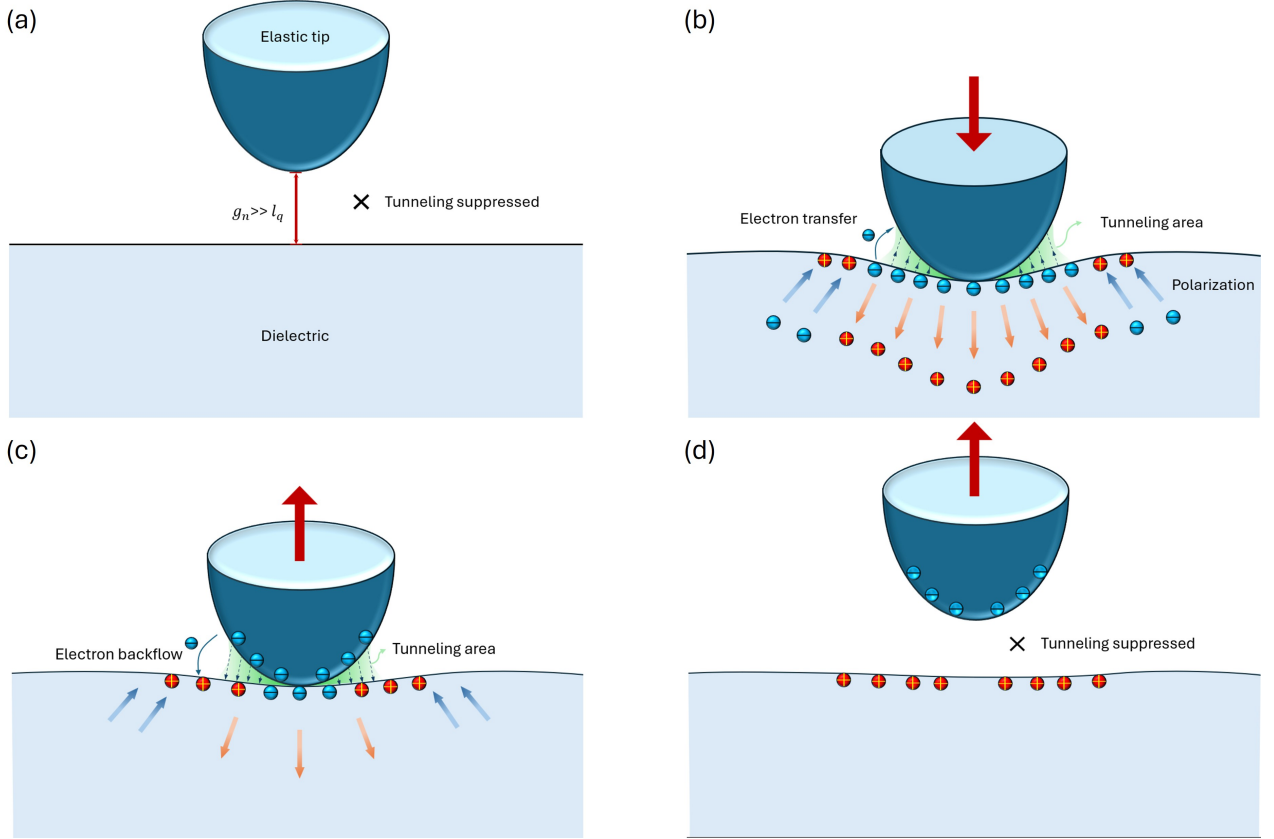


Fig. 2. Schematic of charge transfer in unbiased metal-dielectric contact: (a) large gap with closed tunneling channel; (b) loading with flexoelectric polarization driving charge transfer; (c) unloading with partial charge backflow and edge freezing; (d) complete separation with frozen residual charge.

2.3.3. Metal-dielectric contact: Biased case

When an external voltage V_{tip} is applied to the conducting tip, an additional polarity constraint governs the charge transfer. While an applied bias intrinsically generates a strong capacitive field and potential charge injection, this reversible capacitive charge vanishes upon separation. To systematically isolate the intrinsic electromechanical response, the present model considers only the flexoelectric bound charge as the driving force, treating the tip bias purely as a polarity-selective electron reservoir. Accordingly, the sign of the applied bias determines the polarity of the *net* charge that can accumulate on the dielectric surface: a negatively biased tip preferentially injects electrons, while a positively biased tip preferentially extracts them from dielectric surface states. Although electrons may flow in either direction during any given load step, the net accumulated charge at each surface point is constrained to remain of the bias-determined sign. For instance, electrons injected under negative bias may partially return to the tip during unloading as the flexoelectric demand diminishes. This polarity constraint is the key distinction from the unbiased scenario, where charges of either sign can be transferred to satisfy the full flexoelectric demand.

As defined in Eq. (23), the flexoelectricity-induced polarized surface charge demand is given by $\hat{\sigma}_d^{(n)} = -\mathbf{p}_{\text{flexo}} \cdot \mathbf{n}$. The polarity constraint is then implemented through a projection operator as

$$\Pi_V(x) = \begin{cases} \min(x, 0), & V_{\text{tip}} < 0, \\ x, & V_{\text{tip}} = 0, \\ \max(x, 0), & V_{\text{tip}} > 0. \end{cases} \quad (27)$$

For a negatively biased tip, this projection retains only the negative portion of any quantity, naturally precluding positive charge demands that cannot be satisfied by the electron reservoir. The converse applies for positive bias.

The charge transfer process in the biased case is formulated by applying the polarity constraint to the flexoelectric demand before evaluating the incremental update. Specifically, we define the target charge at step n as

$$\sigma_{\text{tar}}^{(n)} = \Pi_V(\hat{\sigma}_d^{(n)}), \quad (28)$$

where $\sigma_{\text{tar}}^{(n)}$ represents the theoretical maximum charge that the biased tip can supply to meet

the local flexoelectric demand at the current configuration. Substituting σ_{tar} for $\hat{\sigma}_d$ in the incremental update rule (24) yields

$$\Sigma_{\text{froz}}^{(n)} = \Sigma_{\text{froz}}^{(n-1)} + \mathcal{T} \cdot \left(\sigma_{\text{tar}}^{(n)} - \sigma_{\text{tar}}^{(n-1)} \right). \quad (29)$$

The physical insight underlying this formulation becomes clear when comparing with the unbiased case. In unbiased contact, the charge transfer dynamically responds to the symmetric evolution of flexoelectricity. In biased contact, however, both loading and unloading are continuously governed by the asymmetric capacity boundary. When the target decreases during unloading, the frozen charge tracks this capacity contraction as long as the channel remains open. Consequently, this mechanism leads to greater charge recovery during unloading, yielding a residual charge that depends primarily on the channel closing process rather than on the loading history.

Figure 3 illustrates two characteristic stages of biased contact. In the initial contact stage with small contact area, the localized flexoelectric demand leads to high local charge density. As contact progresses and the contact area increases, the charge demand is distributed over a larger region, reducing the local charge density. Notably, for a negatively biased tip, all deposited charges are electrons. Even at the contact periphery where the flexoelectric polarization may reverse sign and create positive charge demand, no positive charges are deposited because of the polarity selectivity of the conducting tip.

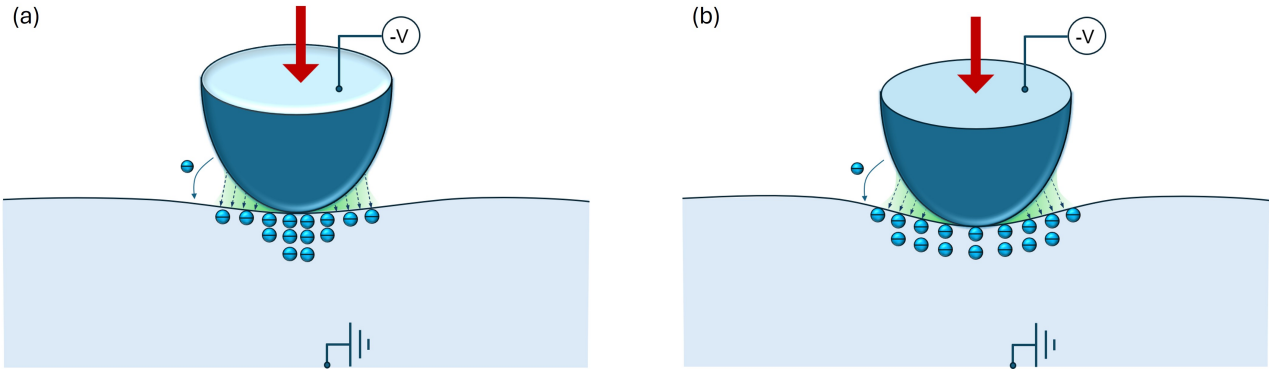


Fig. 3. Schematic of charge transfer in biased metal-dielectric contact (negative tip bias): (a) initial contact with localized high charge density; (b) further contact with distributed lower charge density.

2.3.4. Dielectric-dielectric contact

Contact between two dielectric bodies differs substantially from metal-dielectric contact because neither surface can supply charge freely. Instead, charge transfer relies on surface states: localized electronic levels within the bandgap that arise from lattice termination, defects, or surface contamination [3]. These states act as electron traps with a finite areal density [41]. Several recent experiments support the surface-state mechanism for insulator-insulator electrification: temperature-dependent charge decay follows thermionic emission kinetics, indicating that charges reside in well-defined energy traps [41]; and identical polymers exchange charge when brought into contact with different curvatures, consistent with strain-induced shifts in surface state energy [52]. In the model presented here, we characterize each surface by its maximum trappable charge density σ_{trap} , representing the areal density of available surface states.

When two dielectric surfaces of identical material come into contact, the flexoelectric bound charges $\hat{\sigma}_{b,m}$ and $\hat{\sigma}_{b,s}$ on the master and slave surfaces generally differ due to geometric asymmetry in the strain gradients. This asymmetry alters the local electrostatic environment at the interface, creating an electrochemical potential difference between the surface states on each side and driving electron tunneling until the potential imbalance is neutralized. To estimate the equilibrium transfer, we treat each interfacial point independently and require that the total surface charge be equal on both sides, i.e. $\hat{\sigma}_{b,m} - \Delta\sigma = \hat{\sigma}_{b,s} + \Delta\sigma$, which eliminates the local driving field across the gap: at this point the net unscreened charge is identical on both sides, so neither surface can extract further charge from the other.¹ The idealized amount of charge transferred between the two surfaces is then

$$\Delta\sigma = \frac{\hat{\sigma}_{b,m} - \hat{\sigma}_{b,s}}{2}, \quad (30)$$

where $\hat{\sigma}_{b,m} = \mathbf{p}_{\text{flexo},m} \cdot \mathbf{n}_m$ and $\hat{\sigma}_{b,s} = \mathbf{p}_{\text{flexo},s} \cdot \mathbf{n}_s$ are the flexoelectric bound surface charge densities on the master and slave surfaces, with \mathbf{n}_m and \mathbf{n}_s being the respective outward

¹For contacts between dissimilar dielectrics with different permittivities, this simple halving rule no longer holds, and the equilibrium condition should account for the dielectric mismatch at the interface.

surface normals. The actual transfer is limited by the surface state capacity, expressed as

$$\sigma_{\text{tar}}^{(n)} = \text{sign}(\Delta\sigma^{(n)}) \cdot \min(|\Delta\sigma^{(n)}|, \sigma_{\text{trap}}). \quad (31)$$

In alignment with the framework established above, the charge evolution follows the same incremental update rule:

$$\Sigma_{\text{froz}}^{(n)} = \Sigma_{\text{froz}}^{(n-1)} + \mathcal{T} \cdot \left(\sigma_{\text{tar}}^{(n)} - \sigma_{\text{tar}}^{(n-1)} \right), \quad (32)$$

subject to the physical constraint of finite surface state capacity:

$$\left| \Sigma_{\text{froz}}^{(n)} \right| \leq \sigma_{\text{trap}}. \quad (33)$$

The electrical Neumann contribution follows Eq. (26). This formulation is particularly relevant for contact between identical materials, where geometric asymmetry, such as surface curvature, creates differential strain gradients that drive charge separation despite identical material properties.

2.3.5. Unified charge transfer algorithm

Algorithm 1 collects the charge transfer rules developed in Sections 2.3.2–2.3.4 into a single unified procedure. All three contact scenarios share the same incremental update structure, differing only in the definition of the target charge σ_{tar} . The transparency-weighted incremental rule, the Neumann boundary contribution, and the post-processing steps are common to all cases.

2.4. Variational formulation and discretization

The contact contribution to the weak form arises from the virtual work performed by contact tractions and surface charges at the interface:

$$\delta\Pi_C = \int_{\partial\mathcal{B}_t^C} [t_N \delta g_N + q_C \delta g_\phi] d\gamma, \quad (34)$$

where t_N is the normal contact traction, q_C is the contact surface charge density, and $g_\phi = \phi_s - \bar{\phi}_m$ is the potential gap across the interface, defined analogously to the normal gap g_N . For

Algorithm 1: Unified charge transfer algorithm for contact electrification

Input: Converged fields at step n ; previous frozen charge $\Sigma_{\text{froz}}^{(n-1)}$; previous target $\sigma_{\text{tar}}^{(n-1)}$; contact type

Output: Updated frozen charge $\Sigma_{\text{froz}}^{(n)}$, Neumann contribution $\bar{\omega}^{(n)}$

```
1 foreach integration point on the contact surface do
2   Compute normal gap  $g_N$  from the deformed geometry
3   Compute transparency:  $\mathcal{T} = \frac{1}{1 + \exp(\frac{g_N - \ell_q}{\Delta_g})}$ 
4   switch contact scenario do
5     case Unbiased metal–dielectric do
6        $\hat{\sigma}_d^{(n)} \leftarrow -\mathbf{p}_{\text{flexo}} \cdot \mathbf{n}$ 
7        $\sigma_{\text{tar}}^{(n)} \leftarrow \hat{\sigma}_d^{(n)}$ 
8     case Biased metal–dielectric do
9        $\hat{\sigma}_d^{(n)} \leftarrow -\mathbf{p}_{\text{flexo}} \cdot \mathbf{n}$ 
10       $\sigma_{\text{tar}}^{(n)} \leftarrow \Pi_V(\hat{\sigma}_d^{(n)})$ 
11     case Dielectric–dielectric do
12        $\Delta\sigma^{(n)} \leftarrow \frac{\hat{\sigma}_{b,m}^{(n)} - \hat{\sigma}_{b,s}^{(n)}}{2}$ 
13        $\sigma_{\text{tar}}^{(n)} \leftarrow \text{sign}(\Delta\sigma^{(n)}) \cdot \min(|\Delta\sigma^{(n)}|, \sigma_{\text{trap}})$ 
14     end
15   end
16   Update frozen charge:  $\Sigma_{\text{froz}}^{(n)} \leftarrow \Sigma_{\text{froz}}^{(n-1)} + \mathcal{T} \cdot (\sigma_{\text{tar}}^{(n)} - \sigma_{\text{tar}}^{(n-1)})$ 
17   Compute Neumann contribution:  $\bar{\omega}^{(n)} \leftarrow (1 - \mathcal{T}) \cdot \Sigma_{\text{froz}}^{(n)}$ 
18 end
```

metal-dielectric contact, $\bar{\phi}_m$ reduces to the prescribed metal potential; for dielectric-dielectric contact, it corresponds to the interpolated master surface potential.

The normal contact traction comprises penalty regularization for contact [85] and the adhesive cohesive zone model introduced in Section 2.2:

$$t_N = \begin{cases} \varepsilon_N g_N & \text{if } g_N \leq 0, \\ \frac{\phi_N}{(g_N^{\max})^2} g_N \exp\left(-\frac{g_N}{g_N^{\max}}\right) & \text{if } g_N > 0, \end{cases} \quad (35)$$

where the first case approximates the impenetrability constraint (19) via a large positive penalty parameter ε_N , permitting slight interpenetration ($g_N < 0$) as a trade-off for computational efficiency. The second case applies the adhesive traction (20) during separation.

Analogously, the surface charge density arising from the electrical contact condition (25) takes the penalty form

$$q_C = \varepsilon_\phi \mathcal{T} g_\phi, \quad (36)$$

where ε_ϕ is the electrical penalty parameter, which physically assumes the role of an infinitely large interfacial capacitance per unit area. This constitutive relation strongly penalizes electrical potential jumps, driving the potential gap $g_\phi \rightarrow 0$ at locations where the tunneling channel is open ($\mathcal{T} \approx 1$), thereby enforcing the required local electrostatic equilibrium for transferring compensating charges. It is worth noting that while macroscopic capacitive charge q_C is invoked to equilibrate the potential constraint during contact, it is fully reversible and inherently vanishes upon separation as $\mathcal{T} \rightarrow 0$. The final irreversible surface charge remaining after separation is governed exclusively by the dynamically tracked fraction Σ_{froz} subject to polarity and trap limits.

The contact integrals in (34) are evaluated using isogeometric analysis with NURBS basis functions [69]. The mortar method is employed to project contact quantities onto nodal values via weighted averaging, ensuring smooth transfer of contact forces between non-matching meshes. The resulting coupled electromechanical system is solved using a monolithic Newton–Raphson scheme. The detailed formulation and consistent linearization are provided in Appendix B.

3. Metal-Dielectric AFM Contact

3.1. Problem setup

This section evaluates the model by comparing its predictions with experimental observations in atomic force microscopy (AFM) experiments on polymer substrates. We consider poly(methyl methacrylate) (PMMA) and poly(diallyl phthalate) (PDAP), and contact scenarios including an AFM tip with and without an applied bias. Figure 4 shows the experimental setup and a schematic of the tip-substrate contact. The AFM contact geometry is modeled as an axisymmetric problem, with a metal-coated silicon tip (radius $R = 25$ nm) indenting a finite dielectric substrate. The computational domain is set to $L \times H = 100 \times 100$ nm², which is sufficiently large compared to the contact radius (~ 10 nm) to avoid boundary effects. Complete separation is defined when the minimum normal gap exceeds $2\ell_q$, at which point the tunneling transparency is negligible across the entire interface.

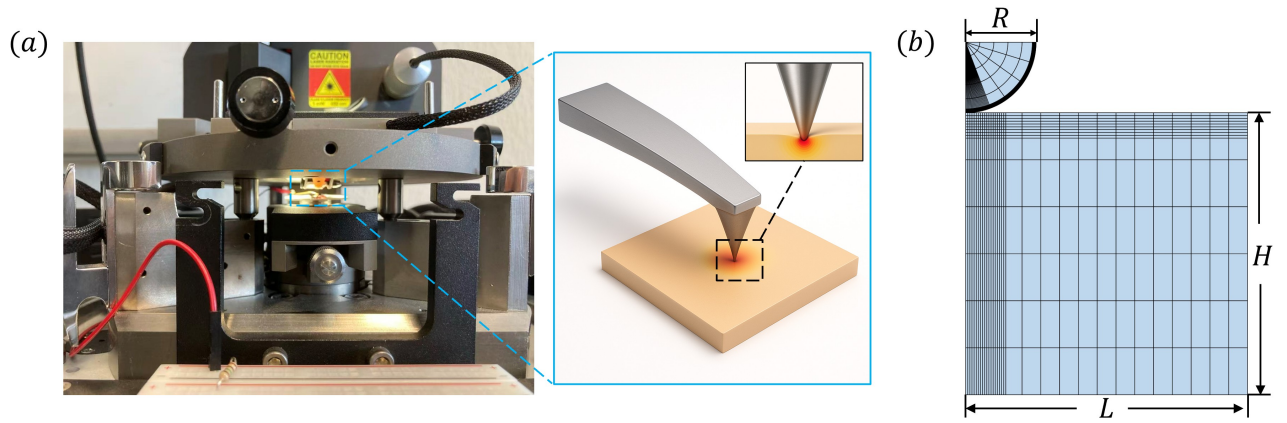


Fig. 4. AFM contact configuration: (a) experimental setup; (b) axisymmetric computational mesh with spherical tip and dielectric substrate.

The material parameters are summarized in Table 1. The mechanical and dielectric properties are obtained from the literature. Flexoelectric coefficients for polymers are not yet routinely measured, and the reported values can span orders of magnitude depending on the measurement technique and sample preparation [86, 87]. Reasonable estimates are therefore adopted based on available measurements and typical polymer values. In particular, the sign of the transverse coefficient μ_T may differ between polymers because it depends on the local molecular polarizability and symmetry of the repeat unit. The signs of the transverse coefficient μ_T are phenomenologically inferred to be opposite for PMMA and PDAP to interpret their contrasting electrification polarities observed in experiments, which serves as a working

assumption in our simulations. A characteristic length of $\ell_s = 0.1$ nm is used for both materials to account for strain gradient elasticity effects. The mechanical penalty parameter is set

Table 1: Material and model parameters.

Parameter	PMMA [88, 89, 90]	PDAP [89, 91]	Tip	Unit
Young's modulus E	3.5	13.0	170	GPa
Poisson's ratio ν	0.36	0.358	0.22	–
Relative permittivity ϵ/ϵ_0	3.6	5.2	–	–
Flexoelectric coeff. μ_L	4.67×10^{-11}	3.62×10^{-11}	–	C/m
Flexoelectric coeff. μ_T	-1.65×10^{-11}	7.95×10^{-11}	–	C/m
Flexoelectric coeff. μ_S	0	1.20×10^{-11}	–	C/m
Adhesion work ϕ_N	5	10	–	J/m ²
Max adhesive traction p_N^{\max}	10	25	–	MPa

to $\varepsilon_N = 10^{10} E$, where E is the Young's modulus of the substrate, and the electrical penalty parameter is evaluated element-wise as $\varepsilon_\phi = \theta \epsilon/h_e$ with $\theta = 0.3$ and h_e the local element size. The resulting maximum interpenetration remains below 0.01 nm, negligible relative to both the contact dimensions and the tunneling length ℓ_q . The AFM simulations use a contact-zone element size $h = 0.29$ nm and a pseudo-time increment $\Delta t = 0.05$. A convergence study confirming the adequacy of these choices is provided in Appendix C.

3.2. Unbiased AFM contact

To verify the mechanical response of the model, we compare the computed contact radius with the classical Hertz theory, as shown in Fig. 5. The figure shows good agreement between the numerical results and the analytical Hertz solution, confirming the accuracy of the contact mechanics implementation. The slight discrepancy above 60 nN is attributed to finite deformation effects and the nonlinear flexoelectric response at large strains.

Figure 6 presents the surface free charge density distribution at the end of the loading phase for different contact forces. It is observed that the two materials exhibit opposite charge patterns due to their different flexoelectric properties. For PMMA, as shown in Fig. 6(a), the contact center exhibits negative charge density while the contact edge shows positive charge. At the contact center, the strain gradient induces positive flexoelectric polarization, attracting negative charges from the metal tip. At the edge, the strain gradient reverses sign due to the local strain field transition from compression to tension, leading to positive charge accumulation. As the contact force increases, the negative charge density at the center initially

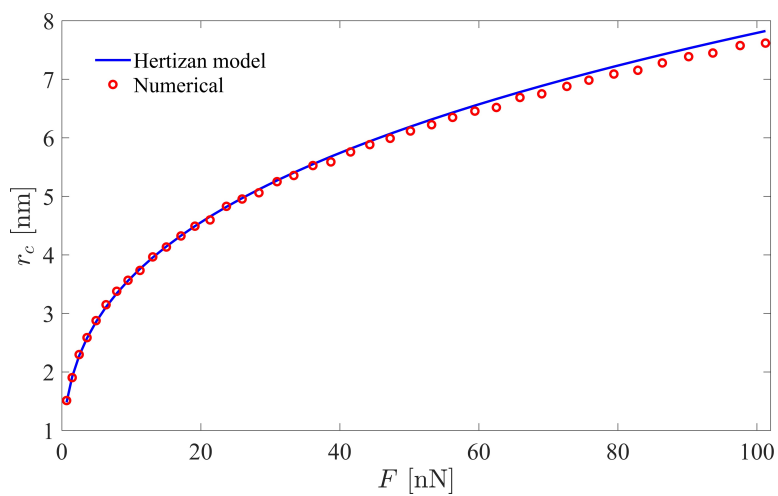


Fig. 5. Contact radius as a function of contact force for PMMA substrate, compared with classical Hertz theory.

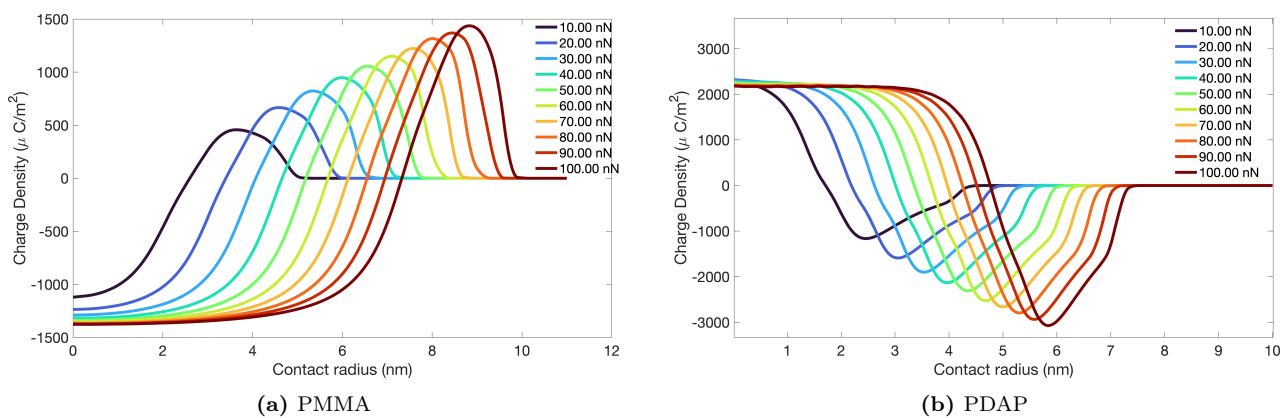


Fig. 6. Surface free charge density distribution at the end of loading for different contact forces: (a) PMMA; (b) PDAP.

increases but then saturates when the strain gradient at the center stops growing. Meanwhile, the positive charge density at the contact edge continues to increase, and the charged region extends outward with the expanding contact area. For PDAP, as shown in Fig. 6(b), the charge polarity is reversed: the contact center shows positive charge density while the edge exhibits negative charge. Within the present model, this opposite pattern arises from the assumed sign of the transverse flexoelectric coefficient μ_T , which governs the polarization response to the dominant strain gradient component.

Figure 7 shows the residual charge distribution after complete separation. In contrast to the loading phase, the contact center region shows nearly zero residual charge, while the original contact edge retains significant charge. This characteristic distribution follows directly from the charge transfer mechanism and the elastic recovery of the substrate. As the mechanical load is removed and the substrate returns to its undeformed shape, the flexoelectric demand at the center diminishes. During unloading, the tunneling channel closes first at the contact periphery where the gap opens earliest, freezing the accumulated charge before it can flow back to the tip. Conversely, the channel at the contact center remains open longest, allowing the charge there to dissipate back to the metal tip to maintain local equilibrium. The final state is thus a ring of frozen charge at the periphery with an uncharged center, which agrees with the theoretical predictions of Silavnieks et al. [78]. It is also worth noting that under the current cohesive parameters, the adhesive effects during unloading do not visibly alter this central discharge behavior.

Notably, the residual charge distributions for different loading forces follow similar spatial profiles, with only the magnitude and extent varying with the maximum contact area. Since PMMA and PDAP exhibit opposite edge charging during loading, the frozen residual charge after separation also displays opposite polarity, as shown in Figs. 7(a) and (b). Figure 8 displays the electric potential distribution at the end of loading and after complete separation for a loading force of 50 nN. The potential field reflects the coupled electromechanical response, with the flexoelectric polarization creating localized potential variations near the contact interface. The potential contours reveal that the field perturbation penetrates approximately 20–30 nm into the substrate. It can be observed that the potential magnitude after separation is significantly reduced.

Figure 9 compares the computed average surface charge density ($\bar{\sigma} = \int_{\gamma_c} \Sigma_{\text{froz}} d\gamma / \int_{\gamma_c} d\gamma$,

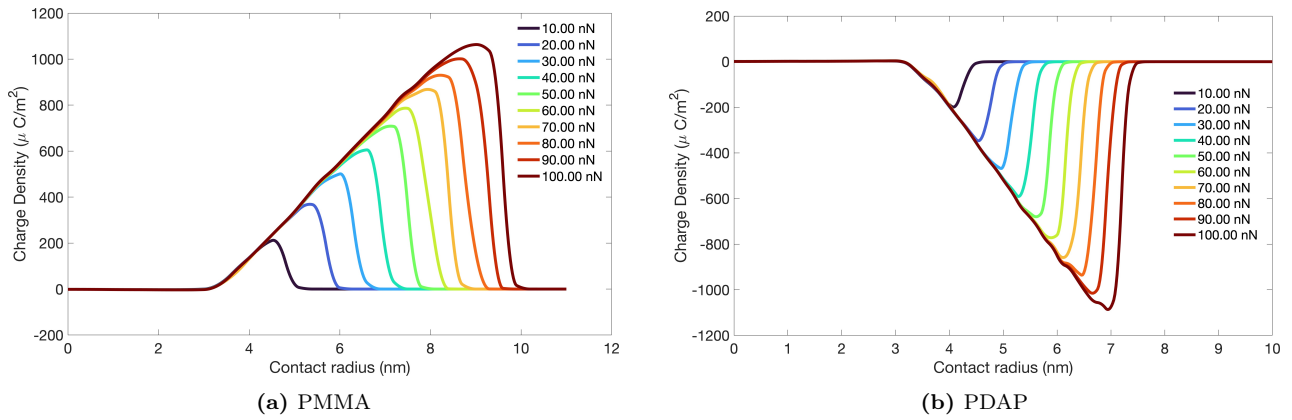


Fig. 7. Residual surface charge density distribution after complete separation for different maximum loading forces: (a) PMMA; (b) PDAP.

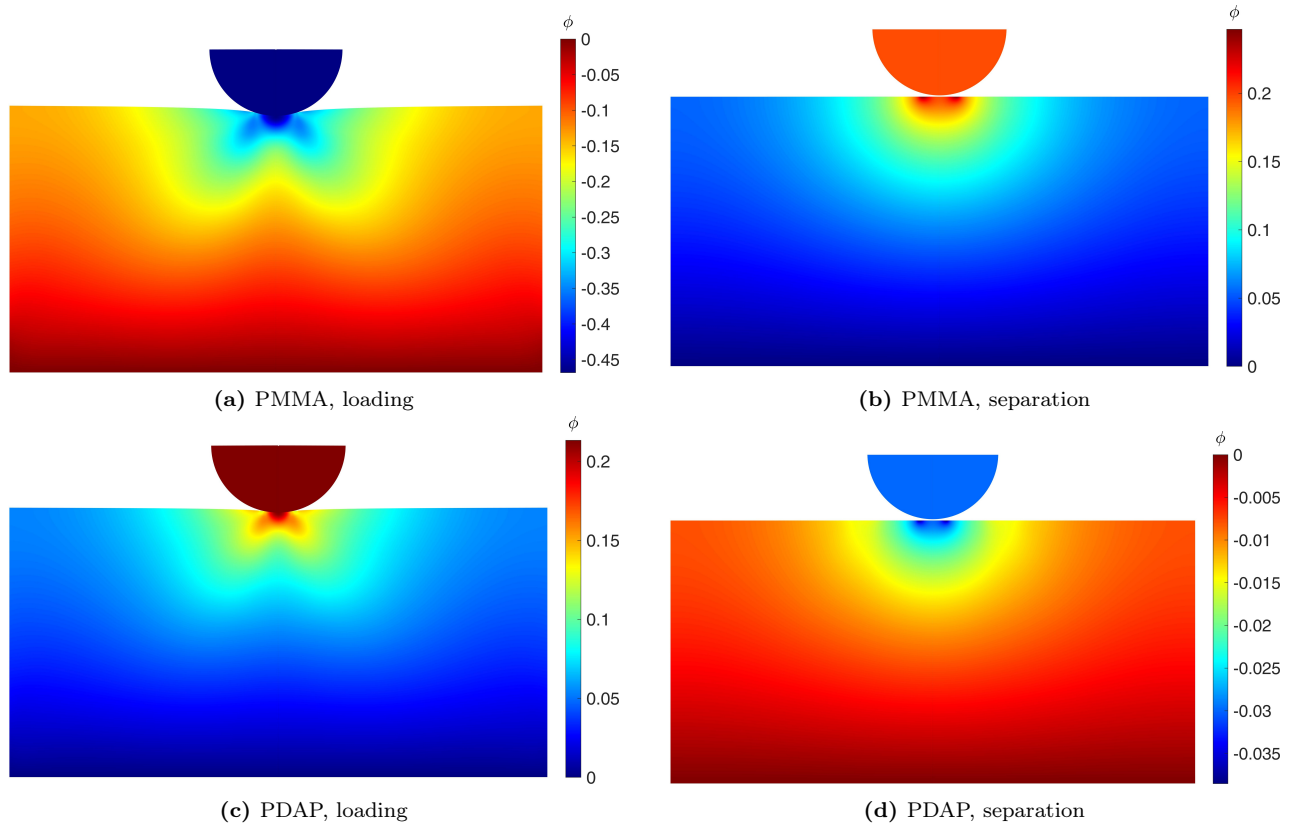


Fig. 8. Electric potential distribution at 50 nN contact force: (a,c) at the end of loading; (b,d) after complete separation.

where γ_c is the total charged area) with experimental data from Lin et al. [32]. The simulation results capture the qualitative trend of increasing charge density with contact force for both PMMA and PDAP, but a quantitative gap is evident. For PDAP at 100 nN, the predicted residual charge density is approximately $300 \mu\text{C}/\text{m}^2$, compared with the measured value of roughly $200 \mu\text{C}/\text{m}^2$, a discrepancy of about a factor of 1.5. For PMMA, the model overestimates by roughly one order of magnitude. Because the charge demand scales linearly with the flexoelectric coefficients, the predicted charge density inherits this linear dependence. Matching the PMMA measurements would therefore require reducing the assumed flexoelectric coefficients by a factor of about 10, placing them at approximately $5 \times 10^{-12} \text{ C}/\text{m}$. Given that measured flexoelectric coefficients for polymers span several orders of magnitude depending on the measurement technique, sample preparation, and loading conditions [86, 87], values in this range remain physically plausible. Additionally, the predicted charge magnitude is related to the strain gradient characteristic length ℓ_s , as larger values of ℓ_s would smooth the localized strain gradients and further reduce the theoretical charge demand. Beyond coefficient uncertainty, other factors may contribute to the discrepancy. At small contact forces, the charge transfer may be partly driven by the intrinsic work function difference between the tip and substrate [33, 31], which is not included in the present model. The Hertzian contact model also assumes an idealized tip geometry that may differ from the actual AFM tip-sample interaction.

3.3. Biased AFM contact

In this section, we investigate the effect of external tip bias on the charge transfer process. The basic setup is the same as in Section 3.2, except that a -4 V tip bias is applied for PMMA and a $+3.2 \text{ V}$ bias for PDAP, matching the experimental conditions of Lin et al. [32]. Figure 10 shows the surface charge distribution at the end of the loading phase. For PMMA, as shown in Fig. 10(a), only negative charges are transferred, with an approximately uniform charge density within the contact region that drops quickly to zero at the contact edge. For PDAP, as shown in Fig. 10(b), only positive charges are transferred, exhibiting a similar plateau distribution. Notably, as shown in the insets, the charge density at the contact center is higher for smaller loading forces, consistent with the mechanism illustrated in Fig. 3, where a smaller contact area leads to a higher local charge density to accommodate the flexoelectric demand.

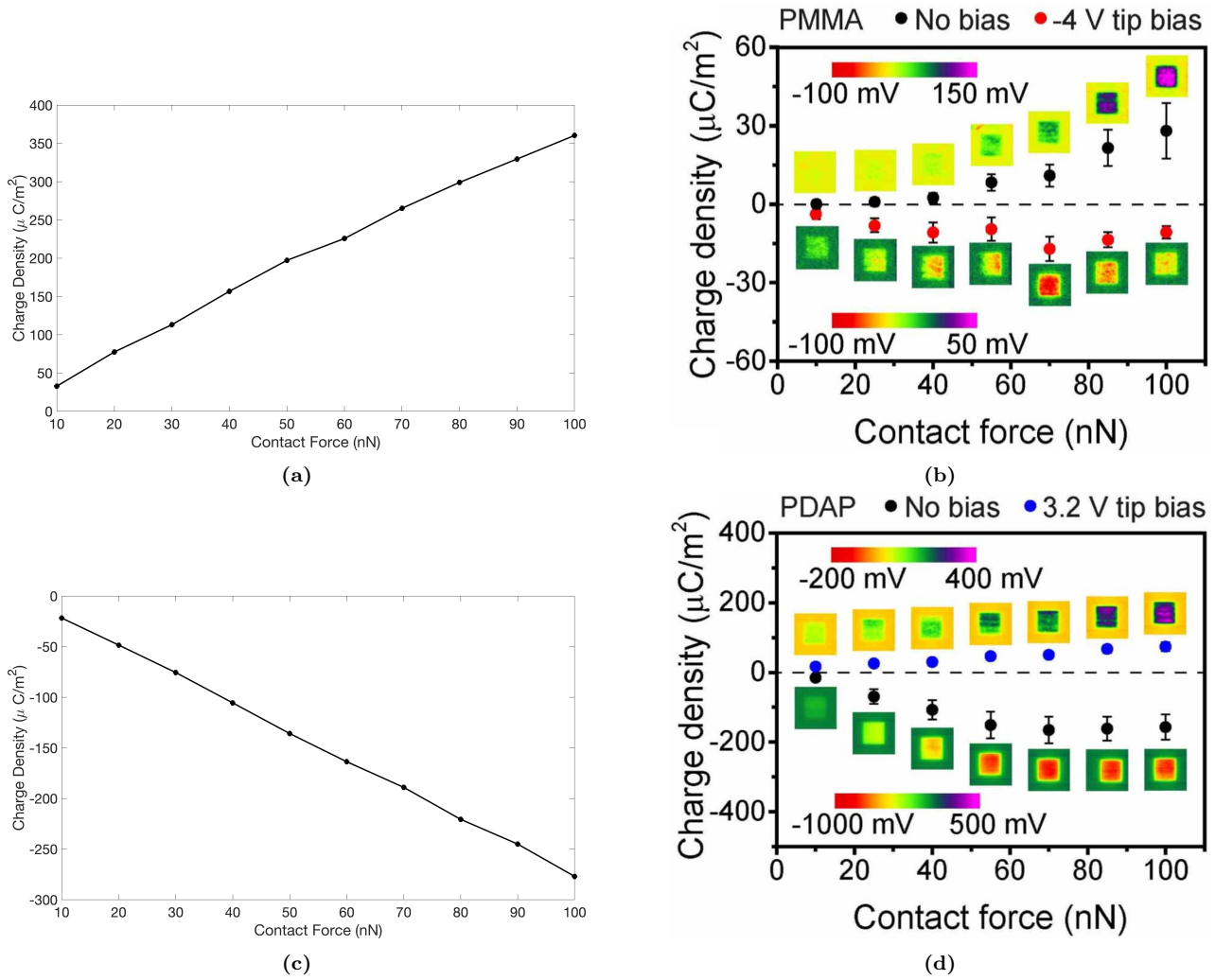


Fig. 9. Comparison of average surface charge density between simulation and experiment: (a,c) simulations for PMMA and PDAP; (b,d) experimental data adapted from Lin et al. [32]. © IOP Publishing. Reproduced with permission. All rights reserved.

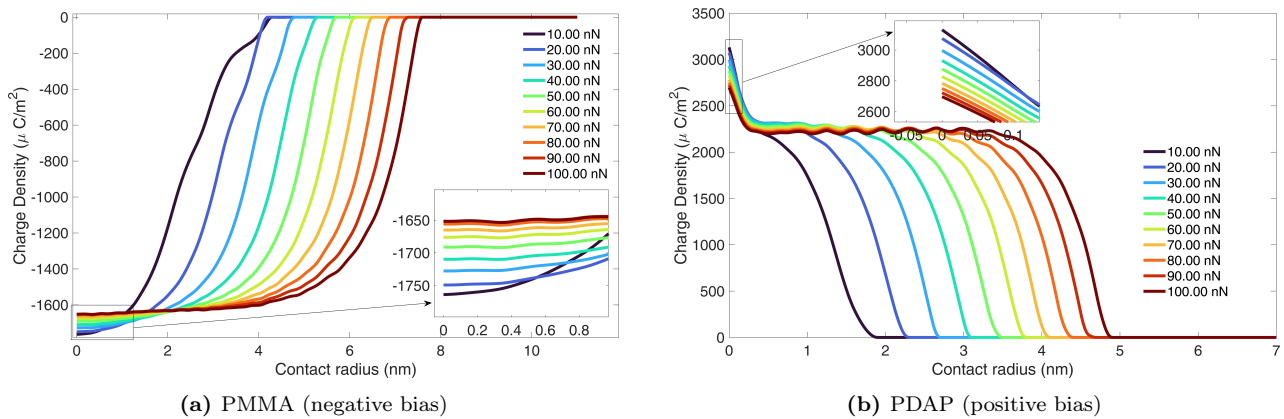


Fig. 10. Surface charge density distribution at the end of loading under biased conditions: (a) PMMA with negative tip bias; (b) PDAP with positive tip bias.

The residual charge distribution after complete separation is shown in Fig. 11. An important feature is that the charge distributions for different loading forces nearly overlap, indicating that the residual charge is almost independent of the maximum loading force. This behavior contrasts with the unbiased case and can be attributed to the single-polarity constraint: because only one polarity of charge can be transferred, the extended contact edge region remains uncharged during loading, resulting in a significantly lower residual charge compared to the unbiased case, where the unrestricted charge supply fully satisfies the bipolar flexoelectric demand, allowing significant peripheral charge of the opposite polarity to freeze upon separation. Figure 12 shows the electric potential distribution at the end of the loading phase and after complete separation for a maximum loading force of 100 nN. The small residual potential after separation, in contrast to the applied bias magnitude during loading, reflects the limited charge transfer through the polarity-restricted pathway.

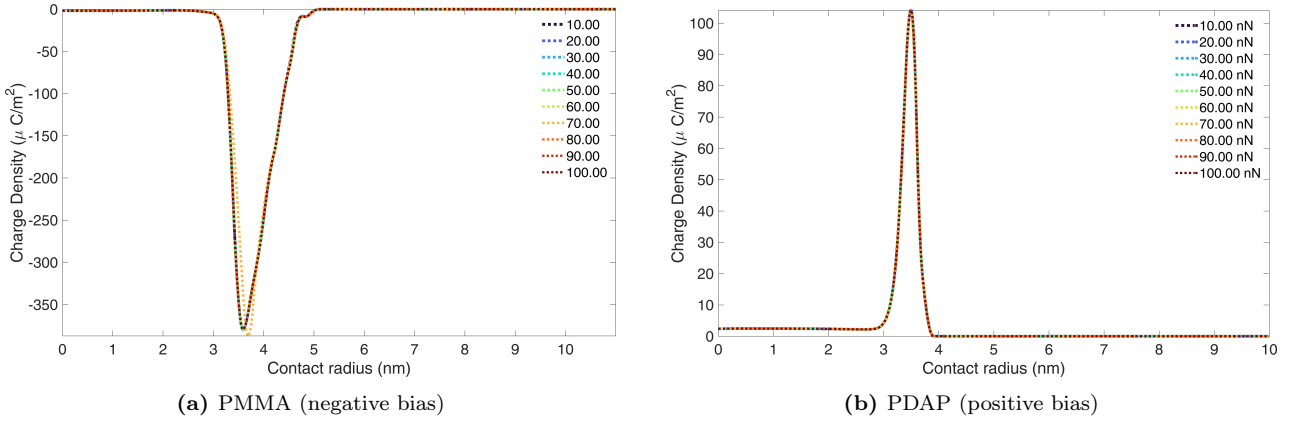


Fig. 11. Residual surface charge density distribution after complete separation under biased conditions: (a) PMMA; (b) PDAP. Note the near-overlap of curves for different loading forces.

The computed average surface charge density for biased contact is shown in Fig. 13 as compared with experimental data in Fig. 9(b,d). The simulation results agree with experimental observations that the magnitude of residual charge density is significantly smaller than in the unbiased case, and the residual charge is nearly independent of the loading force. These features provide strong support for the polarity projection mechanism incorporated in the biased contact model.

3.4. Effect of tip radius and characteristic tunneling length

We further investigate the effect of tip radius R and characteristic tunneling length ℓ_q on the charge distribution, using PDAP in the unbiased contact scenario as a representative case.

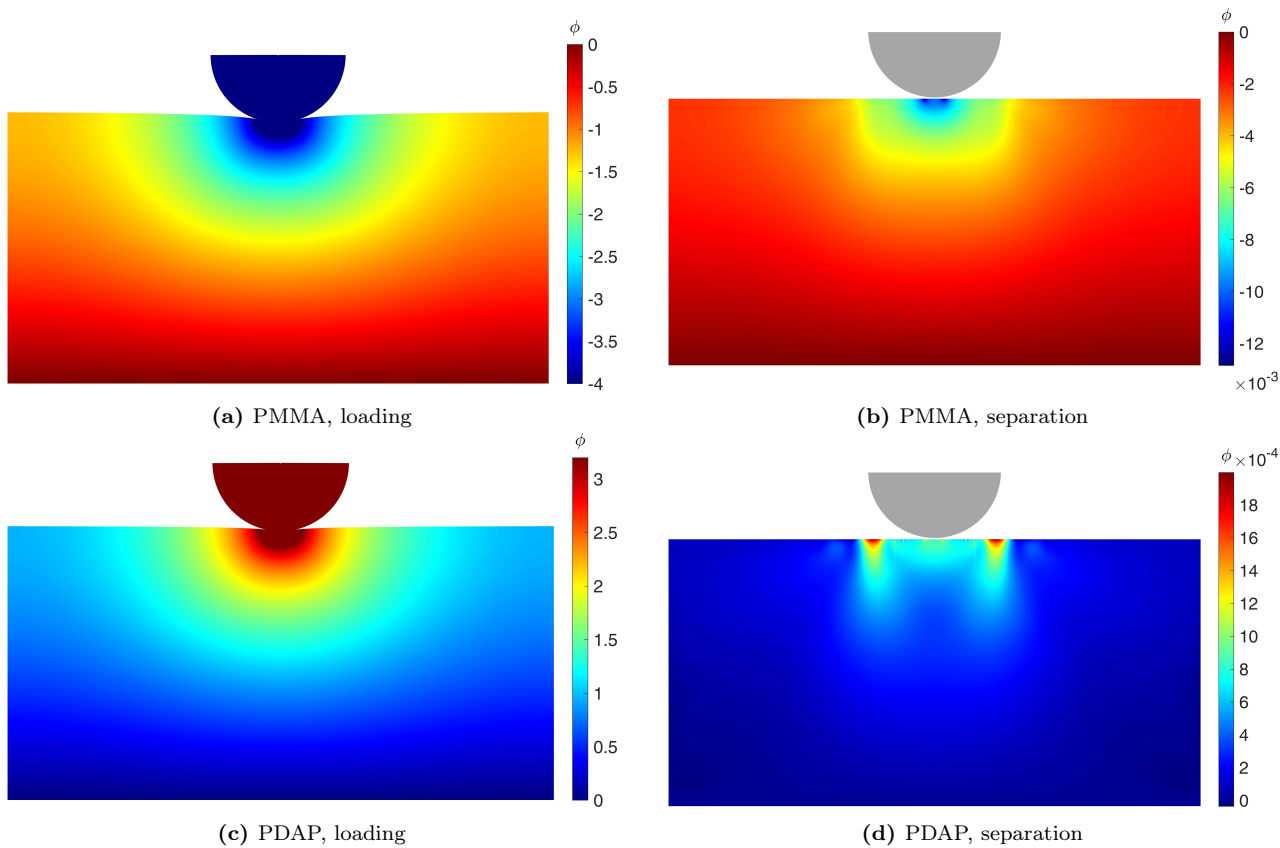


Fig. 12. Electric potential distribution at 100 nN contact force under biased conditions: (a,c) at the end of loading; (b,d) after complete separation.

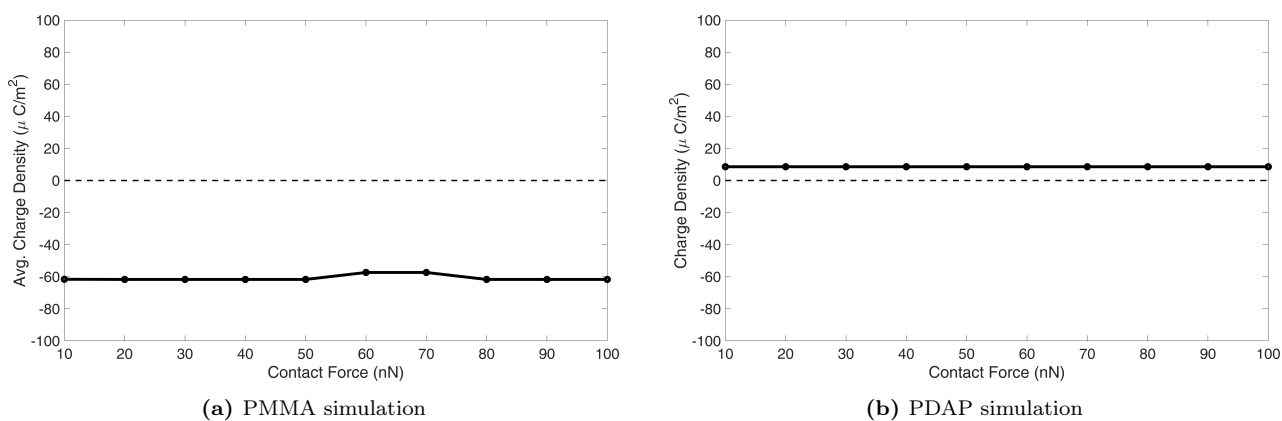


Fig. 13. Average surface charge density as a function of contact force under biased conditions: (a) PMMA; (b) PDAP.

Figure 14 shows the peak charge density when varying the inverse tip radius $1/R$. A clear positive correlation is observed: the peak charge density increases approximately linearly with $1/R$, suggesting that tip sharpness directly correlates with charge density. This trend arises because, for a fixed contact force, a sharper tip not only concentrates the deformation into a smaller contact area but also induces a significantly steeper spatial profile of displacement beneath the indenter. Consequently, local strain gradients are drastically magnified. Since the flexoelectric polarization scales with strain gradient, the driving force for charge transfer is enhanced for sharper tips. The corresponding charge distributions are presented in Fig. 15.

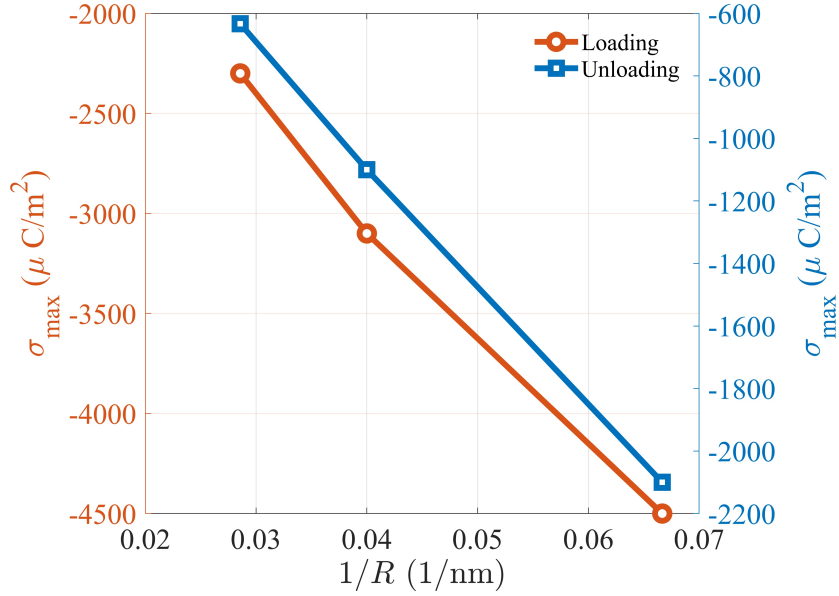


Fig. 14. Peak charge density as a function of inverse tip radius $1/R$ for PDAP in unbiased contact at loading force of 100 nN.

During the loading phase (Fig. 15(a)), the charge profiles exhibit characteristic bipolar patterns for all tip radii, with sharper peaks occurring at smaller R due to the more concentrated strain gradients. After separation (Fig. 15(b)), the residual charge distributions retain similar shapes but with reduced magnitudes, as partial charge backflow occurs during unloading. Notably, the residual charge for larger tips is more spread out laterally due to the larger contact area.

The tunneling length ℓ_q governs how rapidly the charge transfer rate decays with gap distance, as given by Eq. (21). Figure 16 presents the average charge density and charged radius as functions of ℓ_q . The charged radius increases monotonically with ℓ_q , as a larger characteristic length extends the effective range of charge transfer at the contact periphery. In contrast, the magnitude of the average charge density decreases monotonically with increasing

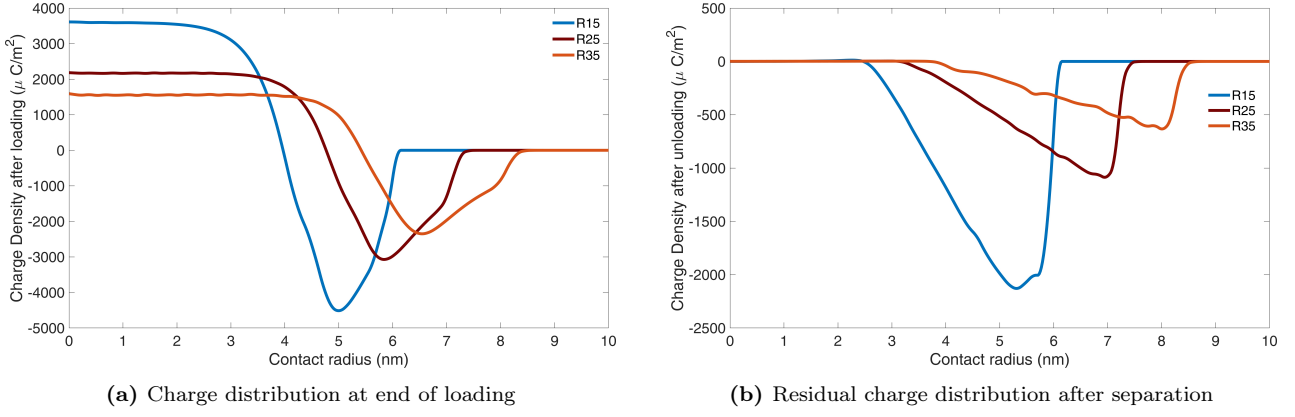


Fig. 15. Spatial charge distributions for varying tip radius R (unit: nm): (a) at maximum indentation; (b) after complete unloading, for PDAP in unbiased contact at loading force of 100 nN.

ℓ_q . This reduction is attributed to the unloading phase: a larger ℓ_q maintains a conductive tunneling channel over larger separation distances, thereby allowing more accumulated charge to flow back before the channel effectively closes. Consequently, a smaller ℓ_q traps surface charge more effectively.

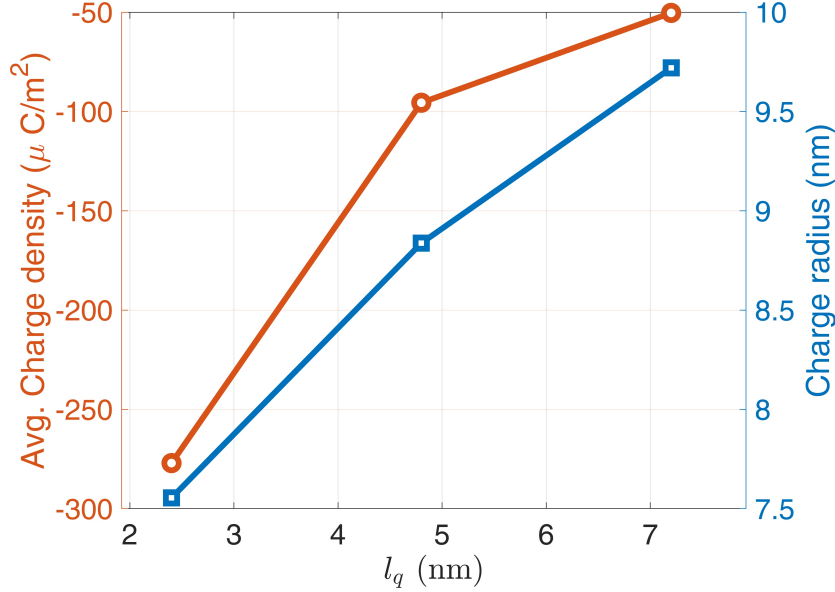


Fig. 16. Average charge density and charged radius as functions of characteristic tunneling length ℓ_q for PDAP at 100 nN contact force.

The spatial profiles in Fig. 17 further illustrate these effects. At maximum loading (Fig. 17(a)), all curves show similar central charge densities, but larger ℓ_q values result in charge distributions that extend further beyond the nominal contact edge. After separation (Fig. 17(b)), smaller ℓ_q values yield higher residual charge because the tunneling channel closes more abruptly upon unloading, thereby "trapping" the charge. In contrast, larger ℓ_q maintains

an open channel longer, allowing more charge to flow back before separation is complete.

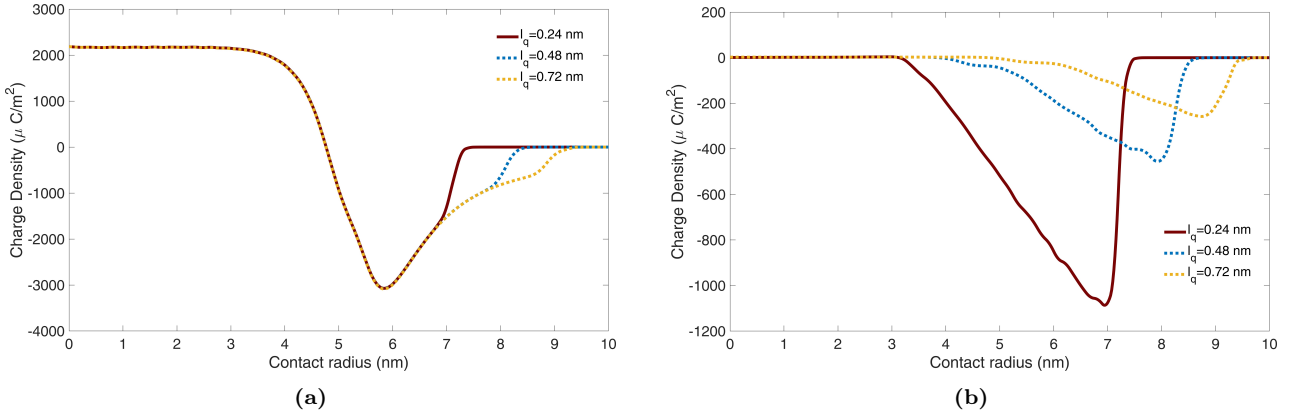


Fig. 17. Spatial charge distributions for varying tunneling length l_q : (a) at maximum indentation; (b) after complete separation for PDAP at 100 nN contact force.

4. Contact Electrification between Identical Dielectrics

Contact electrification between identical materials has long posed a challenge to classical theories because standard electron transfer models rely on intrinsic differences in work function or chemical potential, which are absent across symmetric interfaces [8, 52]. While this phenomenon has been observed for more than a century [92] and extensively studied [93, 94, 95], its underlying mechanism remains debated. Recently, experimental studies [52] have linked charge polarity to local surface curvature, suggesting that the symmetry breaking required for electrification may originate from the physical state of the contact itself. In this section, we apply our computational model to dielectric-dielectric contact electrification and demonstrate that geometric asymmetry combined with flexoelectric effects can induce charge separation even between two contacting bodies with identical material properties.

4.1. Two-dimensional wavy surface contact

We consider contact between a flat lower PMMA body and a wavy upper PMMA body characterized by a wavenumber parameter k that controls the density of asperities. The geometric parameters are set to $L_1 = 70$ nm, $L_2 = 100$ nm, $H = 100$ nm, $A = 5$ nm, with an applied vertical pressure $p_y = 500$ MPa. Figure 18 illustrates the geometry and mesh for a representative wavenumber $k = 1.5$. The simulation employs the same PMMA material parameters as in Section 3, but introduces a surface state capacity parameter $\sigma_{\text{trap}} =$

$100 \mu\text{C}/\text{m}^2$ to impose a physical limit on the maximum transferable charge density at dielectric-dielectric interfaces. This value is conservative relative to the experimentally reported surface state densities of 10^{12} – 10^{13} cm^{-2} [41], and is chosen so that the saturation regime of charge transfer can be reached within the simulated loading conditions.

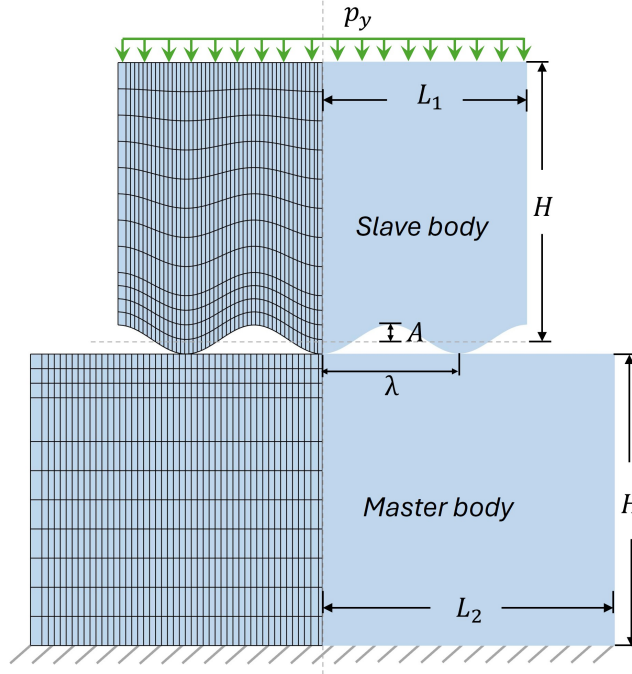


Fig. 18. Schematic of wavy surface contact geometry and mesh (wavenumber $k = L_1/\lambda = 1.5$). The slave body has a wavy surface, while the master body has a flat surface.

The evolution of surface charge distribution during loading reveals how local geometry dictates polarity. Figure 19 presents the charge density profiles at different loading stages for three distinct wavenumbers. For a low wavenumber ($k = 0.5$, Fig. 19(a)), contact is localized at the center. Here, the convex slave surface approaches the flat master surface, inducing a negative charge on the slave and a positive charge on the master. This polarity aligns with the experimental "curvature rule" reported by Xu et al. [52], where they found that convex surfaces in contact acquire negative charge while concave surfaces become positively charged. However, as the wavenumber increases to $k = 1.0$ (Fig. 19(b)), a second contact region emerges at the edge (around 70 nm). The polarity at this edge contact is opposite to that at the center: the master surface gains negative charge while the center remains positive. This spatial variation indicates that charge transfer direction is governed locally by the specific geometric conditions at each contact point rather than by a global material property. At a high wavenumber ($k = 2.0$, Fig. 19(c)), multiple contact points develop, and the charge density

rapidly saturates to the trap limit σ_{trap} . Notably, the global polarity pattern reverses compared to the low wavenumber case, in which the master surface becomes predominantly negatively charged.

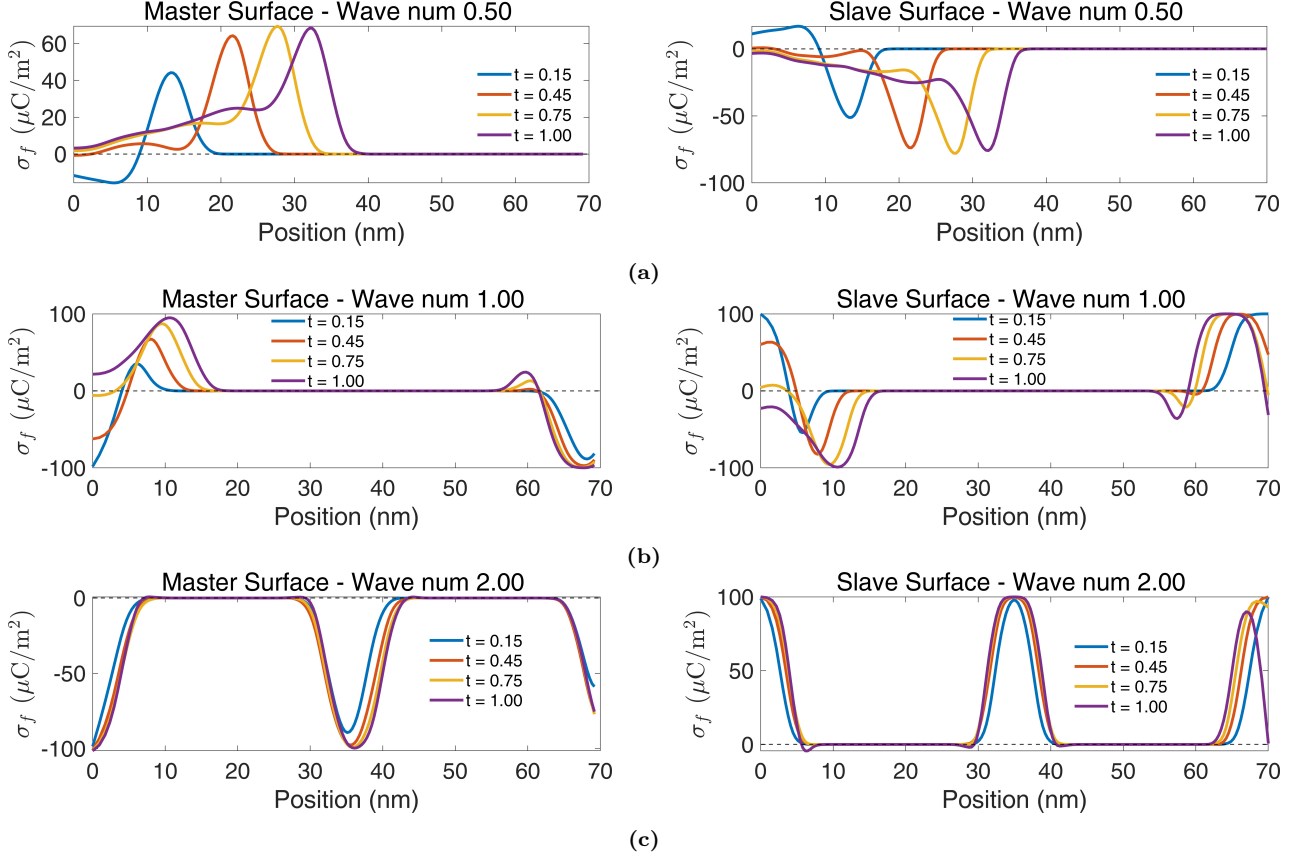


Fig. 19. Surface charge density distribution during loading for different wavenumbers: (a) $k = 0.5$; (b) $k = 1.0$; (c) $k = 2.0$. Upper curves show slave surface; lower curves show master surface.

Upon separation, these charge patterns are largely preserved due to the freezing mechanism. Figure 20 shows the residual charge distributions, where the polarity reversal between the low ($k = 0.5$) and high ($k = 2.0$) wavenumber cases is clearly visible. The corresponding electric potential distributions, shown in Fig. 21, further illustrate the transition from a positive-dominant potential field at low wavenumbers to a negative-dominant field at high wavenumbers.

A systematic analysis of the peak charge density and total charge transferred between surfaces is summarized in Fig. 22. For low wavenumbers ($k < 0.75$), the peak charge density increases monotonically with k , driven by the sharpening of local contact curvature. In the intermediate range ($0.75 < k < 1.5$), the local charge density saturates at the trap limit σ_{trap} . The most significant feature appears in the total charge plot (Fig. 22(b)): a critical transition

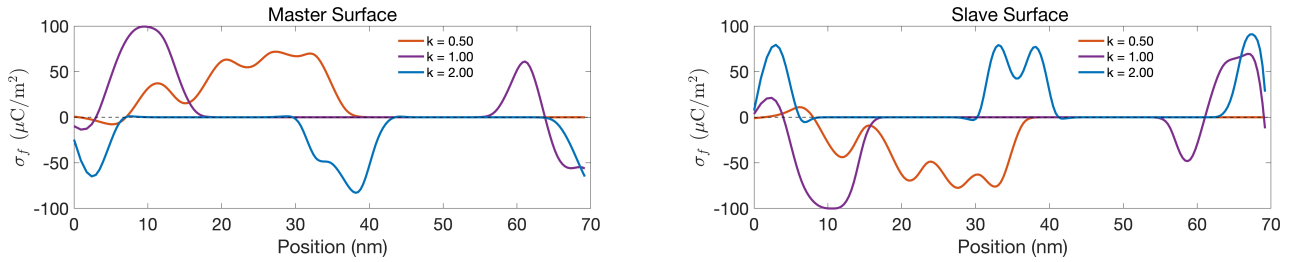


Fig. 20. Residual surface charge density distribution after complete separation for different wavenumbers.

occurs around $k \approx 1.5\text{--}2$, where the net charge on the master surface reverses from positive to negative. This reversal can be understood through the competition between the flexoelectric polarization on the two contacting surfaces. For identical materials, the net charge transfer direction is determined by whichever surface develops a stronger local flexoelectric response. At low wavenumbers, contact occurs at isolated smooth crests where the slave (wavy) surface undergoes larger local deformation, producing a stronger flexoelectric polarization of the appropriate sign that attracts electrons from the master surface. As the wavenumber increases, the asperities become sharper and more densely packed, which intensifies the local deformation on the initially flat master surface. When the master surface's flexoelectric response exceeds that of the slave, the direction of charge transfer reverses, and the master surface becomes the electron acceptor. This finding offers insight into the pressure-dependent polarity reversal observed experimentally [52, 53]. While such reversal has previously been attributed to material transfer or surface damage at high loads [48], our results suggest an alternative mechanism: increasing the wavenumber k sharpens the local asperity curvature, reduces the effective contact area, and increases the true local contact pressure, thereby shifting the balance of flexoelectric response between the two surfaces.

4.2. Three-dimensional random rough surface contact

The wavy surface in the preceding section, while useful for isolating the effect of a single geometric parameter, is an idealization. Real surfaces are randomly rough at the nanoscale, and the resulting charge distributions are correspondingly irregular. To bridge this gap, we now extend the framework to three dimensions and replace the deterministic sinusoid with a stochastic surface profile. The rough surface is generated as a Gaussian random field with prescribed root-mean-square (RMS) amplitude and correlation length l_{corr} , following the methodology in [96].

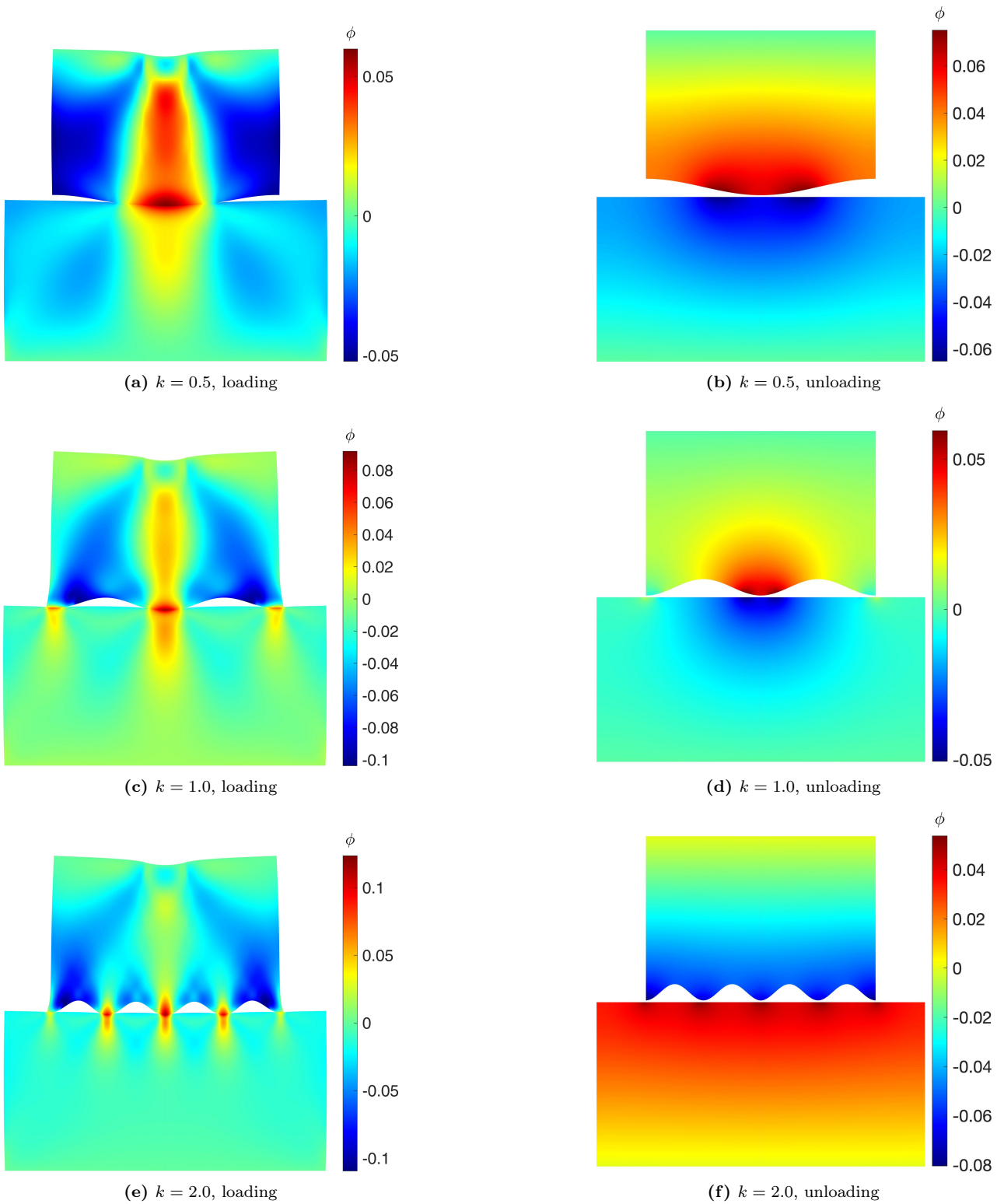


Fig. 21. Electric potential distribution for different wavenumbers: (a,b) $k = 0.5$; (c,d) $k = 1.0$; (e,f) $k = 2.0$. Left column: end of loading; right column: after separation.

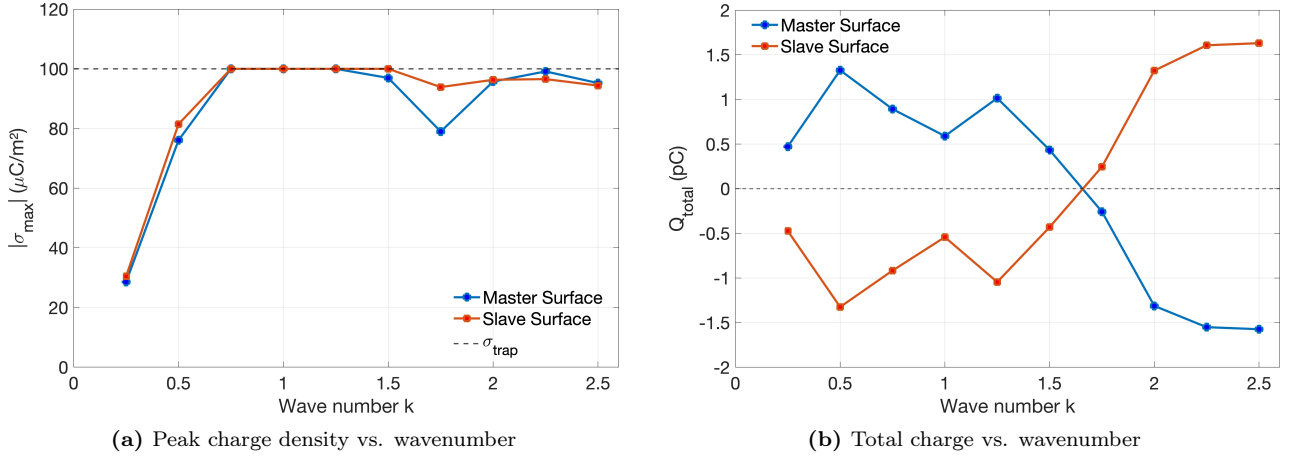


Fig. 22. Quantitative analysis of charge transfer vs. wavenumber: (a) peak charge density on master and slave surfaces; (b) total charge on each surface. Note the polarity reversal around $k \approx 1.5$ – 2 .

The computational domain is shown in Fig. 23. A flat PMMA block of dimensions $100 \times 100 \times 50$ nm is in contact with a smaller PMMA block of dimensions $50 \times 50 \times 50$ nm, whose bottom surface carries the random roughness. The RMS amplitude of the roughness is 0.1 nm. The base of the lower block is fully clamped, while a vertical displacement of $\delta = 8$ nm is prescribed on the top face of the upper block. Both the bottom surface of the lower block and the top surface of the upper block are electrically grounded ($\phi = 0$). After reaching the prescribed displacement, the upper block is gradually retracted until the minimum gap between the two surfaces reaches $20l_q$ (i.e., 4.8 nm), at which point the tunneling channel is fully closed and no further charge transfer occurs.

To study the effect of surface randomness, we vary the correlation length l_{corr} across three values: 6, 10, and 14 nm, while keeping the RMS amplitude fixed. A shorter l_{corr} produces a rougher surface with more frequent, sharper asperities; a longer l_{corr} yields a smoother, more gently undulating profile. The resulting surface topographies are shown in Fig. 24. At $l_{\text{corr}} = 6$ nm, the surface exhibits fine-scale oscillations with peak-to-valley heights spanning roughly 0.5 nm. At $l_{\text{corr}} = 14$ nm, the surface is gentler, with broad hills and shallow valleys.

The residual charge distributions on the master surface after complete separation are shown in Fig. 25 for three independent surface realizations at each correlation length. At $l_{\text{corr}} = 6$ nm, every realization produces a “mosaic” of positive and negative patches scattered across the contact region without obvious spatial order, although the specific patch arrangement differs from one realization to another. When l_{corr} increases to 10 nm, the patches become broader and fewer, and the charge tends to concentrate near the edges of the contact footprint. At

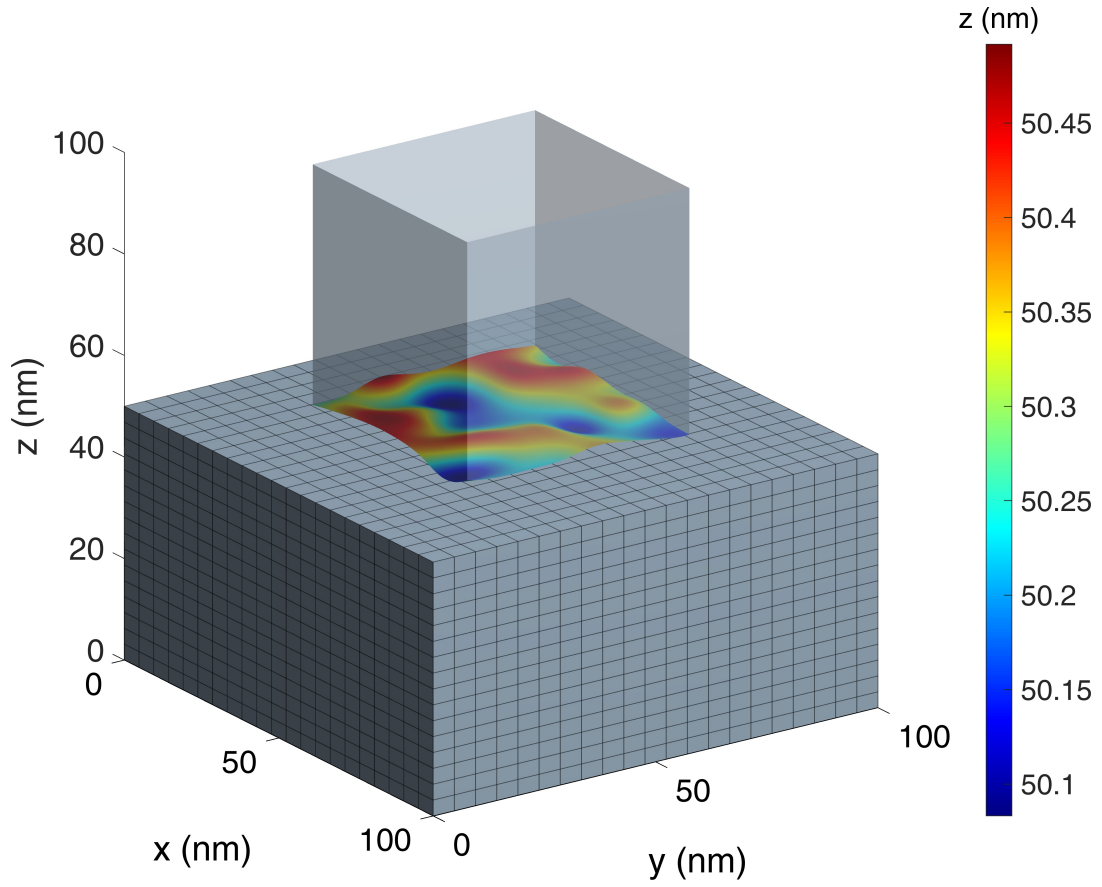


Fig. 23. Geometry of 3D random rough surface contact. The upper block ($50 \times 50 \times 50$ nm) has a randomly rough bottom surface and is pressed into the flat lower block ($100 \times 100 \times 50$ nm). Coloring on the surface indicates the local height variation.

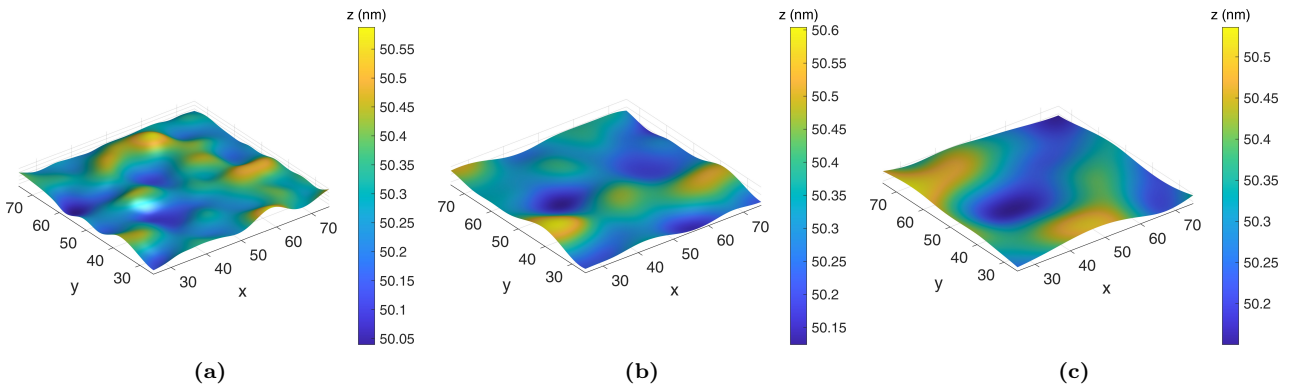


Fig. 24. Random rough surface profiles of the upper body for three correlation lengths: (a) $l_{\text{corr}} = 6$ nm; (b) $l_{\text{corr}} = 10$ nm; (c) $l_{\text{corr}} = 14$ nm. Shorter l_{corr} corresponds to finer, more irregular roughness.

$l_{\text{corr}} = 14$ nm, the mosaic character disappears in all three realizations: intense negative bands run along the contact edges while the interior carries only a weak, nearly uniform negative charge. The consistency of these trends across independent realizations indicates that they are governed by the correlation length of the roughness rather than by the details of any single random surface.

These results can be explained through the mechanism of flexoelectric polarization competition established in Section 4.1. For contact between identical dielectrics, the local electrification polarity depends on which surface undergoes more intensive local deformation and consequently develops a stronger flexoelectric response. On a highly irregular surface with a short correlation length, the dominant flexoelectric response shifts rapidly between the upper and lower bodies across the contact interface. This spatial alternation in polarization dominance yields an irregular “mosaic” of positive and negative charge patches, with dimensions that scale with the roughness correlation length. As l_{corr} increases, the surface profile becomes smoother and the contact-induced local strain gradients become more uniform. Consequently, the charge distribution aggregates into distinct, macroscopic regions rather than a scattered mosaic.

Notably, these results are consistent with the “mosaic charge” pattern reported by Baytekin et al. [95], who observed that nominally identical polymer surfaces develop spatially heterogeneous charge distributions upon contact. Their experiments ruled out bulk material differences as the cause, but left the physical mechanism unresolved. Our simulations show that flexoelectricity, combined with nanoscale surface roughness, is sufficient to reproduce this effect. The random topography ensures that local deformation is distributed unequally between the two contacting bodies. This asymmetry in localized strain drives an unbalanced flexoelectric response across the interface, resulting in a spatially heterogeneous charge transfer without the need for material inhomogeneity or chemical asymmetry.

To assess how robust these observations are, we repeat the simulation with ten independent random surface realizations for each correlation length and collect per-realization charge statistics. Figure 26(a) shows the peak positive and peak negative charge densities on the master surface, averaged over the ten realizations, as a function of l_{corr} . The peak positive charge density $|\sigma_+|$ stays between 28 and 33 $\mu\text{C}/\text{m}^2$ across the three correlation lengths, while $|\sigma_-|$ is roughly half that, around 13–16 $\mu\text{C}/\text{m}^2$. This asymmetry is attributed to the geomet-

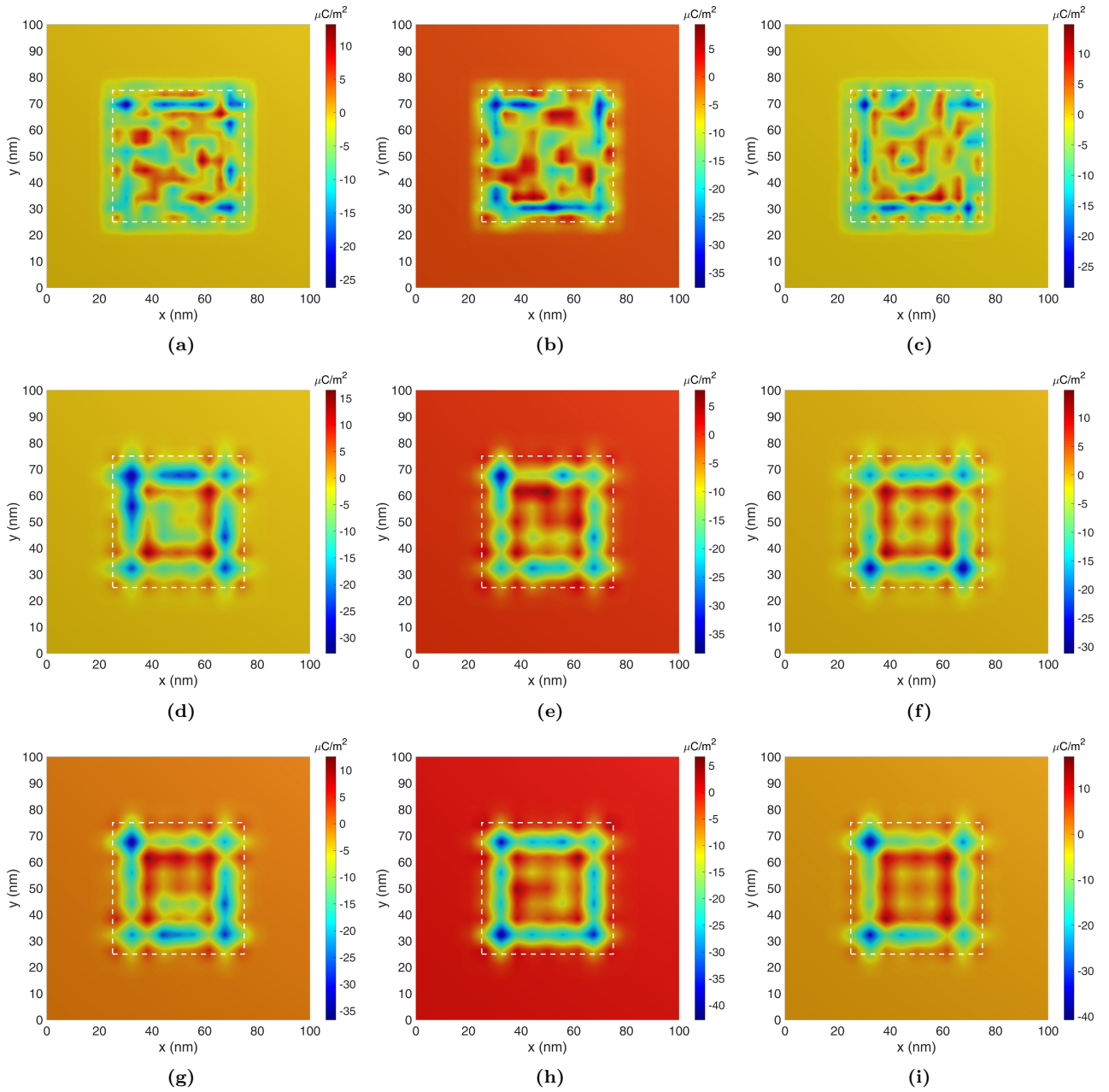


Fig. 25. Residual charge distribution on the master surface after separation for three correlation lengths and three independent surface realizations. Rows from top to bottom: $l_{\text{corr}} = 6, 10,$ and 14 nm. Columns correspond to different random seeds. The dashed rectangle marks the footprint of the slave block. Shorter l_{corr} produces a more pronounced “mosaic” of alternating positive and negative charge, and this trend is consistent across all realizations.

ric asymmetry between the slave and master blocks. Neither quantity shows a statistically significant dependence on l_{corr} , which is reasonable because the RMS amplitude is fixed and hence the overall contact force distribution remains similar across correlation lengths. What changes with l_{corr} is the spatial arrangement of charge, not its magnitude. The total residual charge Q_{total} on the master surface, shown in Fig. 26(b), tells a complementary story. Because the positive and negative charge patches in each realization nearly cancel, Q_{total} is several orders of magnitude smaller than the peak densities. Its mean value shows a weak decreasing trend from roughly 1.5×10^{-5} fC at $l_{\text{corr}} = 6$ nm to about 1.0×10^{-5} fC at 14 nm, though the large inter-realization variance renders this trend statistically insignificant. In other words, the peak charge density is a sample-robust quantity, whereas the net charge on each surface is sensitive to the specific random geometry.

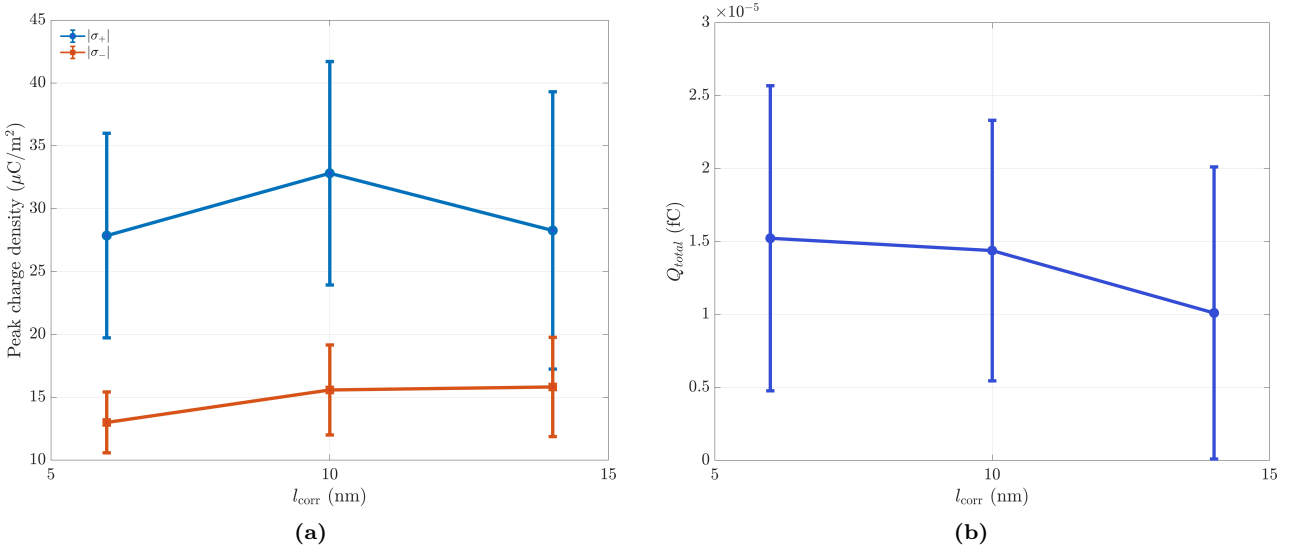


Fig. 26. Statistics of residual charge across ten random surface realizations for each l_{corr} . (a) Peak positive ($|\sigma_+|$) and peak negative ($|\sigma_-|$) charge density vs. l_{corr} . (b) Total residual charge Q_{total} on the master surface vs. l_{corr} .

5. Discussion

5.1. Limitations and assumptions

The present model assumes quasi-static loading and unloading throughout, so dynamic and rate-dependent effects that may arise during high-speed contacts are not captured. All simulations are performed at room temperature, and the temperature dependence of tunneling probability, surface state occupation, and material stiffness is neglected. A further simplification is that only electron transfer driven by flexoelectric polarization is considered. Ion transfer

and material transfer, both of which may contribute under certain experimental conditions, lie outside the scope of this framework.

The flexoelectric coefficients used for the polymer substrates deserve particular attention. These coefficients are not well characterized experimentally for most polymers, and the values adopted here are assumed within a physically reasonable range rather than taken from independent measurements. As demonstrated in Section 3.2, the predicted charge density is linear in the flexoelectric coefficients, so the discrepancy with experiment, which ranges from a factor of 1.5 for PDAP to about one order of magnitude for PMMA, can be primarily attributed to the uncertainty in the assumed values of these material parameters. The qualitative trends, spatial patterns, and force dependence predicted by the model are independent of the coefficient magnitude and are therefore more robust conclusions than the absolute charge densities. Direct experimental measurement of the full flexoelectric tensor for the polymers of interest would substantially reduce this uncertainty and enable quantitative predictions.

Finally, the dielectric-dielectric contact model assumes a spatially uniform surface state density. Real polymer surfaces exhibit defects, contamination, and processing-induced heterogeneity that could modulate the local tunneling rate and charge capacity. Incorporating a spatially varying surface state distribution is a natural extension for future work.

5.2. Comparison with existing models

Two recent models have addressed the role of flexoelectricity in contact electrification, each from a different angle. Silavnieks et al. [78] derived an analytical expression for flexoelectric charge transfer at a Hertzian contact, including the unloading phase and the resulting residual charge. Their closed-form scaling laws offer physical transparency but are limited to smooth, axisymmetric geometries without adhesion. Olson and Marks [50] modeled metal-semiconductor junctions with depletion layers, focusing on Schottky barrier modulation by flexoelectric fields. The numerical model developed in this work complements these approaches by treating arbitrary surface topographies, including the 3D random rough surfaces, and by targeting polymer dielectrics with surface states across the full loading-unloading cycle.

Beyond these two works, the present computational model introduces two features that, to our knowledge, have not appeared in previous literature. First, by incorporating a tunneling transparency function that regulates charge transfer based on the local interfacial gap, the model captures both the evolution of charge accumulation during loading and its irreversible

freezing during separation, without relying on any cut-off criteria. Second, the model provides a unified theoretical treatment for diverse contact scenarios. The identical multiphysics formulation successfully simulates unbiased metal-dielectric contact, biased metal-dielectric contact, and contact between identical dielectrics, differing only in the applied boundary conditions and material parameters. This unified approach makes it possible to systematically compare charging phenomena across widely different experimental configurations within a single, consistent framework.

6. Conclusions

This work presents a computational model for contact electrification that fully couples finite-deformation flexoelectric theory, contact mechanics with cohesive-zone adhesion, and physics-based charge transfer rules. A central element of the model is the tunneling transparency function, which regulates the charge transfer channel based on the local interfacial gap throughout the loading-unloading cycle. During separation, the gap opens earliest at the contact periphery, causing the tunneling channel to close progressively inward. This naturally captures the irreversible trapping of surface charge and produces residual charge patterns after separation.

Three contact scenarios have been investigated within the same formulation. In unbiased metal-dielectric contact, the spatial variation of strain gradients beneath a spherical indenter produces a characteristic bipolar charge pattern on PMMA and PDAP substrates, with one polarity at the contact center and the opposite at the edge. After separation, residual charge concentrates at the original contact periphery, and its magnitude increases with contact force, both trends consistent with the AFM measurements of Lin et al. [32]. Parametric studies further show that peak charge density scales linearly with inverse tip radius, and that a shorter tunneling length traps more charge by closing the tunneling channel more abruptly. When a voltage bias is applied to the tip, the projection mechanism restricts charge transfer to carriers of a single sign. This polarity restriction suppresses edge charging and produces residual charge that is nearly independent of the applied force, again in qualitative agreement with experiment.

The same model has been applied to contact between identical dielectric bodies, yielding new physical insights. In two-dimensional simulations with a wavy surface, the net charge

polarity on each body reverses at a critical wavenumber. This reversal is driven by a shift in which contacting surface undergoes the more intensive local deformation, thus determining which body develops the dominant flexoelectric response. This polarity reversal offers a geometric explanation for the pressure-dependent charge reversal observed in experiments [52, 53]. Three-dimensional simulations on random rough surfaces demonstrate that the spatial scale of the resulting charge mosaic tracks the correlation length of the roughness: short correlation lengths produce fine, randomly interspersed positive and negative patches, consistent with the mosaic charge patterns first reported by Baytekin et al. [95]. Statistical analysis over multiple random realizations shows that the peak charge density is robust across surface realizations, while the net charge on each surface is sensitive to the specific geometry, reflecting near-cancellation of the positive and negative contributions. These results establish that flexoelectric polarization combined with nanoscale geometric heterogeneity is sufficient to produce spatially non-uniform charge distributions between chemically identical surfaces, without requiring any material inhomogeneity.

Several questions remain open for future investigation. Because the predicted charge density scales linearly with the flexoelectric coefficients, the quantitative accuracy of the model hinges on independent measurements of these coefficients for the polymers of interest. Dedicated experiments to determine the full flexoelectric tensor would therefore be a prerequisite for moving from the qualitative trends demonstrated here to quantitative predictions. Extensions to dynamic loading conditions, temperature-dependent tunneling, and competing transfer mechanisms such as ion and material transfer would broaden the range of applicability.

Appendix A. Detailed representation of higher-order boundary tractions

The terms $\tilde{\mathbf{T}}^t$ and $\tilde{\mathbf{T}}^n$ in the higher-order mechanical boundary conditions originate from the surface boundary integral during integration by parts. The surface gradient operator $D_J^{(t)}$ is defined by splitting the variation $\delta\chi$ into tangential and normal gradient components as follows:

$$\begin{aligned}\delta\chi_{k,J} &= D_J^{(t)}\delta\chi_k + N_J D^{(n)}\delta\chi_k, \\ D_J^{(t)} &\equiv (\delta_{JL} - N_J N_L)\partial_L, \\ D^{(n)} &\equiv N_L\partial_L.\end{aligned}\tag{A.1}$$

Consequently, the final formulation of the traction surface projections $\tilde{\mathbf{T}}^t$ and $\tilde{\mathbf{T}}^n$ in index notation can be obtained as

$$\begin{aligned}\tilde{T}_k^{(t)} &= \frac{1}{2} \left[\Sigma_{IJK} N_K (N_J \chi_{k,I} + N_I \chi_{k,J}) D_L^{(t)} N_L - N_K (\chi_{k,I} D_J^{(t)} \Sigma_{IJK} + \chi_{k,J} D_I^{(t)} \Sigma_{IJK}) \right. \\ &\quad \left. - \Sigma_{IJK} (\chi_{k,I} D_J^{(t)} N_K + \chi_{k,J} D_I^{(t)} N_K) \right], \\ \tilde{T}_k^{(n)} &= \frac{1}{2} \Sigma_{IJK} N_K (\chi_{k,I} N_J + \chi_{k,J} N_I).\end{aligned}\tag{A.2}$$

Appendix B. Contact Mechanics Implementation

This appendix presents the detailed contact formulation in a general three-dimensional setting, including surface parametrization, mortar treatment, and consistent linearization. Greek indices $\alpha, \beta \in \{1, 2\}$ denote surface parametric directions, with summation implied over repeated indices.

Appendix B.1. Surface parametrization

The master contact surface is parametrized by convective coordinates $\boldsymbol{\xi}^\alpha = (\xi^1, \xi^2)$. The covariant tangent vectors and unit normal are defined as

$$\boldsymbol{\tau}_\alpha = \frac{\partial \bar{\mathbf{x}}^m}{\partial \xi^\alpha}, \quad \mathbf{n} = \frac{\boldsymbol{\tau}_1 \times \boldsymbol{\tau}_2}{\|\boldsymbol{\tau}_1 \times \boldsymbol{\tau}_2\|},\tag{B.1}$$

where $\bar{\mathbf{x}}^m = \bar{\mathbf{x}}^m(\boldsymbol{\xi}^\alpha)$ denotes the position on the master surface. The metric tensor $m_{\alpha\beta}$ (with its contravariant inverse denoted as $m^{\alpha\beta}$) and curvature tensor $k_{\alpha\beta}$ are defined as

$$m_{\alpha\beta} = \boldsymbol{\tau}_\alpha \cdot \boldsymbol{\tau}_\beta, \quad k_{\alpha\beta} = \bar{\mathbf{x}}_{,\alpha\beta}^m \cdot \mathbf{n}.\tag{B.2}$$

For each slave point \mathbf{x}^s , the closest point projection onto the master surface determines the projection parameter $\bar{\boldsymbol{\xi}}^\alpha$ through

$$(\mathbf{x}^s - \bar{\mathbf{x}}^m) \cdot \boldsymbol{\tau}_\alpha \Big|_{\bar{\boldsymbol{\xi}}^\alpha} = 0.\tag{B.3}$$

The normal gap is $g_N = (\mathbf{x}^s - \bar{\mathbf{x}}^m) \cdot \mathbf{n}$, and the potential gap is $g_\phi = \phi_s - \bar{\phi}_m$, where $\bar{\phi}_m = \phi^m(\bar{\boldsymbol{\xi}}^\alpha)$ is the master potential at the projection point.

Appendix B.2. Variations and consistent linearization

The variation of the normal gap is

$$\delta g_N = (\delta \mathbf{u}^s - \delta \bar{\mathbf{u}}^m) \cdot \mathbf{n}. \quad (\text{B.4})$$

The variation of the projection parameter is obtained from the stationarity condition:

$$\delta \bar{\xi}^\alpha = (m_{\alpha\beta} - g_N k_{\alpha\beta})^{-1} [(\delta \mathbf{u}^s - \delta \bar{\mathbf{u}}^m) \cdot \boldsymbol{\tau}_\beta + g_N \mathbf{n} \cdot \delta \bar{\mathbf{u}}_{,\beta}^m]. \quad (\text{B.5})$$

For the potential gap:

$$\delta g_\phi = \delta \phi_s - \delta \bar{\phi}_m - \bar{\phi}_{,\alpha}^m \delta \bar{\xi}^\alpha, \quad (\text{B.6})$$

where $\bar{\phi}_{,\alpha}^m = \partial \phi^m / \partial \xi^\alpha$ evaluated at the projection point.

For Newton–Raphson iteration, consistent linearization requires the second variation. From standard contact mechanics [85]:

$$\begin{aligned} \Delta \delta g_N = & - (\delta \bar{\mathbf{u}}_{,\alpha}^m \Delta \bar{\xi}^\alpha + \Delta \bar{\mathbf{u}}_{,\alpha}^m \delta \bar{\xi}^\alpha + \bar{\mathbf{x}}_{,\alpha\beta}^m \delta \bar{\xi}^\alpha \Delta \bar{\xi}^\beta) \cdot \mathbf{n} \\ & + g_N m^{\alpha\beta} (\delta \bar{\mathbf{u}}_{,\alpha}^m + \bar{\mathbf{x}}_{,\alpha\gamma}^m \delta \bar{\xi}^\gamma) \mathbf{n} \otimes \mathbf{n} (\Delta \bar{\mathbf{u}}_{,\beta}^m + \bar{\mathbf{x}}_{,\beta\delta}^m \Delta \bar{\xi}^\delta). \end{aligned} \quad (\text{B.7})$$

Appendix B.3. Mortar treatment

The mortar method projects local contact quantities onto nodal values via weighted averaging with NURBS basis functions R_A . For each control point A , the nodal gap, transparency, and potential gap are

$$g_{NA} = \frac{\int_{\partial \mathcal{B}_t^C} R_A g_N \, d\gamma}{A_A}, \quad \mathcal{T}_A = \frac{\int_{\partial \mathcal{B}_t^C} R_A \mathcal{T} \, d\gamma}{A_A}, \quad g_{\phi A} = \frac{\int_{\partial \mathcal{B}_t^C} R_A g_\phi \, d\gamma}{A_A}, \quad (\text{B.8})$$

where $A_A = \int_{\partial \mathcal{B}_t^C} R_A \, d\gamma$ is the tributary area. The nodal contact traction and surface charge are:

$$t_{NA} = \begin{cases} \varepsilon_N g_{NA} & \text{if } g_{NA} \leq 0, \\ \frac{\phi_N}{(g_N^{\max})^2} g_{NA} \exp\left(-\frac{g_{NA}}{g_N^{\max}}\right) & \text{if } g_{NA} > 0, \end{cases} \quad q_{CA} = \varepsilon_\phi \mathcal{T}_A g_{\phi A}. \quad (\text{B.9})$$

The first case of t_{NA} approximates impenetrability via penalty, while the second applies the adhesive cohesive traction (20).

The contact virtual work (34) can then be expressed in mortar form as

$$\delta \bar{\Pi}_C = \sum_A (t_{NA} \delta g_{NA} + q_{CA} \delta g_{\phi A}) A_A. \quad (\text{B.10})$$

Appendix B.4. NURBS discretization

Let the element contain n_e^s slave and n_e^m master control points. We define the following discretization vectors by assembling slave and master contributions:

$$\mathbf{N}^e = \begin{bmatrix} R_1^s \mathbf{n} \\ \vdots \\ R_{n_e^s}^s \mathbf{n} \\ -R_1^m \mathbf{n} \\ \vdots \\ -R_{n_e^m}^m \mathbf{n} \end{bmatrix}, \quad \mathbf{T}_\alpha^e = \begin{bmatrix} R_1^s \boldsymbol{\tau}_\alpha \\ \vdots \\ R_{n_e^s}^s \boldsymbol{\tau}_\alpha \\ -R_1^m \boldsymbol{\tau}_\alpha \\ \vdots \\ -R_{n_e^m}^m \boldsymbol{\tau}_\alpha \end{bmatrix}, \quad \mathbf{P}^e = \begin{bmatrix} R_1^s \\ \vdots \\ R_{n_e^s}^s \\ -R_1^m \\ \vdots \\ -R_{n_e^m}^m \end{bmatrix}, \quad (\text{B.11})$$

where shape functions are evaluated at the slave point and its master projection, respectively.

The parameter gradient vectors involve only master shape function derivatives:

$$\mathbf{N}_\alpha^e = \begin{bmatrix} \mathbf{0} \\ \vdots \\ \mathbf{0} \\ -R_{1,\alpha}^m \mathbf{n} \\ \vdots \\ -R_{n_e^m,\alpha}^m \mathbf{n} \end{bmatrix}. \quad (\text{B.12})$$

The parametric response vector, derived from (B.5), captures the change in projection parameters due to displacement variations:

$$\mathbf{D}_\alpha^e = (m_{\alpha\beta} - g_N k_{\alpha\beta})^{-1} (\mathbf{T}_\beta^e - g_N \mathbf{N}_\beta^e). \quad (\text{B.13})$$

The geometric coupling vector accounts for curvature effects in the normal direction:

$$\bar{\mathbf{N}}_\alpha^e = \mathbf{N}_\alpha^e - k_{\alpha\beta} \mathbf{D}_\beta^e. \quad (\text{B.14})$$

Appendix B.5. Tangent stiffness matrices

The contact contribution to the tangent stiffness matrix is obtained by substituting the discretized variations into the linearized weak form. Denoting the geometric stiffness contribution as $\mathbf{K}_C^{uu,geo}$, the mechanical block comprises both material and geometric contributions:

$$\mathbf{K}_C^{uu} = \sum_A \left[\frac{\varepsilon_N^A}{A_A} \int_{\partial\mathcal{B}_t^C} R_A \mathbf{N}^e d\gamma \int_{\partial\mathcal{B}_t^C} R_A \mathbf{N}^{eT} d\gamma + \int_{\partial\mathcal{B}_t^C} \varepsilon_N^A g_{NA} R_A \left(g_N m^{\alpha\beta} \bar{\mathbf{N}}_\alpha^e \bar{\mathbf{N}}_\beta^{eT} + \mathbf{D}_\alpha^e \mathbf{N}_\alpha^{eT} + \mathbf{N}_\alpha^e \mathbf{D}_\alpha^{eT} - k_{\alpha\beta} \mathbf{D}_\alpha^e \mathbf{D}_\beta^{eT} \right) d\gamma \right], \quad (\text{B.15})$$

where the effective stiffness ε_N^A switches between penalty and adhesive contributions:

$$\varepsilon_N^A = \begin{cases} \varepsilon_N & \text{if } g_{NA} \leq 0, \\ \frac{\phi_N}{(g_N^{\max})^2} \left(1 - \frac{g_{NA}}{g_N^{\max}} \right) \exp\left(-\frac{g_{NA}}{g_N^{\max}}\right) & \text{if } g_{NA} > 0. \end{cases} \quad (\text{B.16})$$

The electrical block is

$$\mathbf{K}_C^{\phi\phi} = \sum_A \frac{\varepsilon_\phi \mathcal{T}_A}{A_A} \int_{\partial\mathcal{B}_t^C} R_A \mathbf{P}^e d\gamma \int_{\partial\mathcal{B}_t^C} R_A \mathbf{P}^{eT} d\gamma. \quad (\text{B.17})$$

The internal force vectors are

$$\mathbf{F}_C^u = \sum_A t_{NA} \int_{\partial\mathcal{B}_t^C} R_A \mathbf{N}^e d\gamma, \quad \mathbf{F}_C^\phi = \sum_A q_{CA} \int_{\partial\mathcal{B}_t^C} R_A \mathbf{P}^e d\gamma. \quad (\text{B.18})$$

Remark. For two-dimensional problems, the surface reduces to a curve with a single parameter $\xi^1 = \xi$. The metric tensor becomes the scalar $m_{11} = \|\boldsymbol{\tau}_1\|^2$ and the curvature reduces to $k_{11} = \bar{\mathbf{x}}_{,\xi\xi}^m \cdot \mathbf{n}$. All tensorial expressions collapse accordingly.

Appendix C. Mesh and Load-Step Convergence

To verify that the numerical results are independent of the spatial and pseudo-time step discretization, we perform a convergence study for the representative case of unbiased PMMA contact at a loading force of 50 nN. Figure C.27 shows the surface charge density at the end of loading for six successively refined meshes. The profiles for $h = 0.29$ nm and $h = 0.24$ nm are

virtually indistinguishable, confirming that the adopted mesh captures the charge distribution with sufficient accuracy. Figure C.28 presents the residual charge density after complete separation for four pseudo-time increments. The curves for $\Delta t = 0.05$ and $\Delta t = 0.04$ largely overlap, indicating that the chosen step size introduces no substantial discretization error.

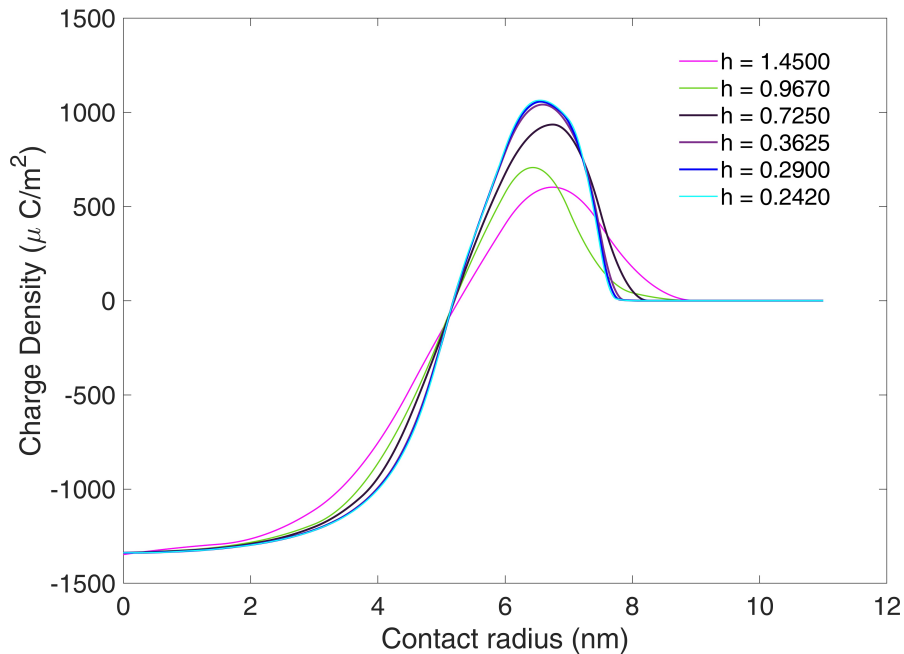


Fig. C.27. Mesh convergence of the surface charge density at the end of loading for unbiased PMMA contact at 50 nN. The element size h (in nm) refers to the contact-zone mesh.

References

- [1] Z. L. Wang, A. C. Wang, On the origin of contact-electrification, *Materials Today* 30 (2019) 34–51. doi:10.1016/j.mattod.2019.05.016.
- [2] S. Pan, Z. Zhang, Fundamental theories and basic principles of triboelectric effect: A review, *Friction* 7 (1) (2019) 2–17. doi:10.1007/s40544-018-0217-7.
- [3] J. Lowell, A. C. Rose-Innes, Contact electrification, *Advances in Physics* 29 (6) (1980) 947–1023. doi:10.1080/00018738000101466.
- [4] W. R. Harper, *Contact and Frictional Electrification*, Clarendon Press, Oxford, 1967.

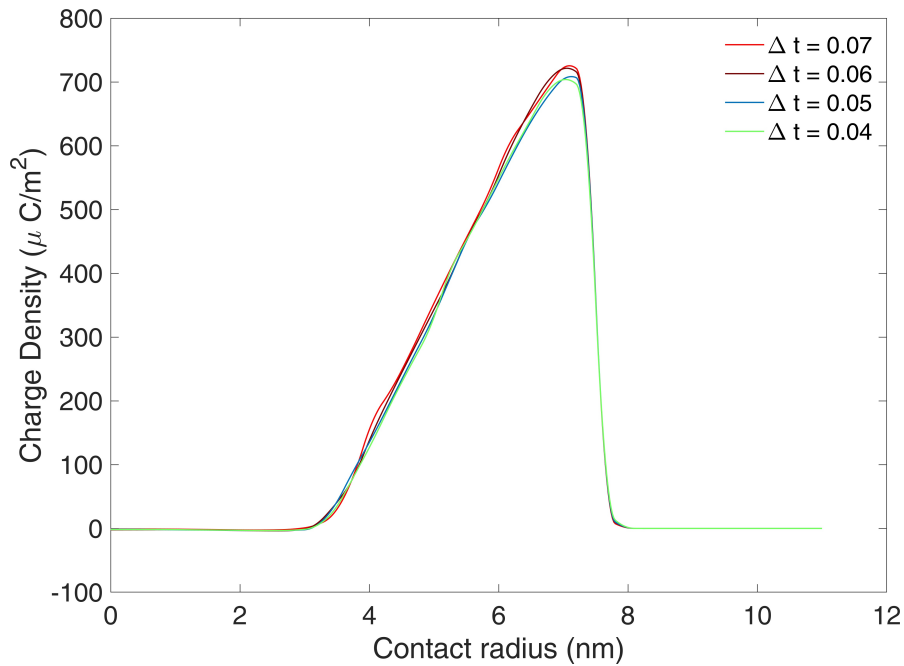


Fig. C.28. Load-step convergence of the residual charge density for unbiased PMMA contact at 50 nN. Δt is the pseudo-time increment.

- [5] J. Wong, P. C. L. Kwok, H.-K. Chan, Electrostatics in pharmaceutical solids, *Chemical Engineering Science* 125 (2015) 225–237. doi:10.1016/j.ces.2014.05.037.
- [6] L. B. Schein, *Electrophotography and Development Physics*, 3rd Edition, Springer Science & Business Media, 2013. doi:10.1007/978-3-642-77744-8.
- [7] C. Saunders, Charge separation mechanisms in clouds, *Space Science Reviews* 137 (1) (2008) 335–353. doi:10.1007/s11214-008-9345-0.
- [8] D. J. Lacks, R. M. Sankaran, Contact electrification of insulating materials, *Journal of Physics D: Applied Physics* 44 (45) (2011) 453001. doi:10.1088/0022-3727/44/45/453001.
- [9] W. D. Greason, *Electrostatic Damage in Electronics: Devices and Systems*, Research Studies Press, Letchworth, 1987.
- [10] M. Glor, Hazards due to electrostatic charging of powders, *Journal of Electrostatics* 16 (2-3) (1985) 175–191. doi:10.1016/0304-3886(85)90041-5.
- [11] S. Matsusaka, H. Maruyama, T. Matsuyama, M. Ghadiri, Triboelectric charging of

- powders: A review, *Chemical Engineering Science* 65 (22) (2010) 5781–5807. doi:10.1016/j.ces.2010.07.005.
- [12] F.-R. Fan, Z.-Q. Tian, Z. L. Wang, Flexible triboelectric generator, *Nano Energy* 1 (2) (2012) 328–334. doi:10.1016/j.nanoen.2012.01.004.
- [13] Z. L. Wang, Triboelectric nanogenerator (TENG)—sparking an energy and sensor revolution, *Advanced Energy Materials* 10 (17) (2020) 2000137. doi:10.1002/aenm.202000137.
- [14] Y. Zi, S. Niu, J. Wang, Z. Wen, W. Tang, Z. L. Wang, Standards and figure-of-merits for quantifying the performance of triboelectric nanogenerators, *Nature Communications* 6 (1) (2015) 8376. doi:10.1038/ncomms9376.
- [15] B. Chen, Y. Yang, Z. L. Wang, Scavenging wind energy by triboelectric nanogenerators, *Advanced Energy Materials* 8 (10) (2018) 1702649. doi:10.1002/aenm.201702649.
- [16] J. Wang, S. Li, F. Yi, Y. Zi, J. Lin, X. Wang, Y. Xu, Z. L. Wang, Sustainably powering wearable electronics solely by biomechanical energy, *Nature communications* 7 (1) (2016) 12744. doi:10.1038/ncomms12744.
- [17] Z. L. Wang, J. Chen, L. Lin, Progress in triboelectric nanogenerators as a new energy technology and self-powered sensors, *Energy & Environmental Science* 8 (8) (2015) 2250–2282. doi:10.1039/C5EE01532D.
- [18] T. Cheng, H. Hu, N. Valizadeh, L. Qiong, F. Bittner, L. Yang, T. Rabczuk, X. Jiang, X. Zhuang, The influence of discontinuity-induced fringing effect on the output performance of contact-separation mode triboelectric nanogenerators: Experiment and modeling studies, *Advanced Energy and Sustainability Research* 5 (10) (2024) 2400002. doi:10.1002/aesr.202400002.
- [19] L. Liu, X. Guo, C. Lee, Promoting smart cities into the 5G era with multi-field internet of things (IoT) applications powered with advanced mechanical energy harvesters, *Nano Energy* 88 (2021) 106304. doi:10.1016/j.nanoen.2021.106304.
- [20] F. Yi, Z. Zhang, Z. Kang, Q. Liao, Y. Zhang, Recent advances in triboelectric nanogenerator-based health monitoring, *Advanced Functional Materials* 29 (41) (2019) 1808849. doi:10.1002/adfm.201808849.

- [21] R. D. I. G. Dharmasena, K. Jayawardena, C. Mills, J. Deane, J. Anguita, R. Dorey, S. Silva, Triboelectric nanogenerators: providing a fundamental framework, *Energy & Environmental Science* 10 (8) (2017) 1801–1811. doi:10.1039/C7EE01139C.
- [22] J. Tian, F. Wang, Y. Ding, R. Lei, Y. Shi, X. Tao, S. Li, Y. Yang, X. Chen, Self-powered room-temperature ethanol sensor based on brush-shaped triboelectric nanogenerator, *Research* (2021). doi:10.34133/2021/8564780.
- [23] L. Xu, T. Jiang, P. Lin, J. J. Shao, C. He, W. Zhong, X. Y. Chen, Z. L. Wang, Coupled triboelectric nanogenerator networks for efficient water wave energy harvesting, *ACS nano* 12 (2) (2018) 1849–1858. doi:10.1021/acsnano.7b08674.
- [24] Y. Zi, J. Wang, S. Wang, S. Li, Z. Wen, H. Guo, Z. L. Wang, Effective energy storage from a triboelectric nanogenerator, *Nature Communications* 7 (1) (2016) 10987. doi:10.1038/ncomms10987.
- [25] T. Cheng, J. Shao, Z. L. Wang, Triboelectric nanogenerators, *Nature Reviews Methods Primers* 3 (1) (2023) 39. doi:10.1038/s43586-023-00220-3.
- [26] C. Cao, Z. Li, F. Shen, Q. Zhang, Y. Gong, H. Guo, Y. Peng, Z. L. Wang, Progress in techniques for improving the output performance of triboelectric nanogenerators, *Energy & Environmental Science* 17 (3) (2024) 885–924. doi:10.1039/D3EE03520D.
- [27] H. Zou, Y. Zhang, L. Guo, P. Wang, X. He, G. Dai, H. Zheng, C. Chen, A. C. Wang, C. Xu, et al., Quantifying the triboelectric series, *Nature Communications* 10 (1) (2019) 1427. doi:10.1038/s41467-019-09461-x.
- [28] Q. Chen, H. Shang, B. Cheng, C. Lu, Y. Wang, Y. Zhang, T. Shao, Quantifying triboelectric series of polymers based on the measurement of triboelectrification with nacl solution, *Chemical Engineering Journal* 488 (2024) 150871. doi:10.1016/j.cej.2024.150871.
- [29] C. A. Mizzi, A. Y. W. Lin, L. D. Marks, Does flexoelectricity drive triboelectricity?, *Physical Review Letters* 123 (11) (2019) 116103. doi:10.1103/PhysRevLett.123.116103.
- [30] B. Persson, On the role of flexoelectricity in triboelectricity for randomly rough surfaces, *Europhysics Letters* 129 (1) (2020) 10006. doi:10.1209/0295-5075/129/10006.

- [31] K. P. Olson, C. A. Mizzi, L. D. Marks, Band bending and ratcheting explain triboelectricity in a flexoelectric contact diode, *Nano Letters* 22 (10) (2022) 3914–3921. doi:10.1021/acs.nanolett.2c00107.
- [32] S. Lin, M. Zheng, L. Xu, L. Zhu, Z. L. Wang, Electron transfer driven by tip-induced flexoelectricity in contact electrification, *Journal of Physics D: Applied Physics* 55 (31) (2022) 315502. doi:10.1088/1361-6463/ac6f2e.
- [33] H. Qiao, P. Zhao, O. Kwon, A. Sohn, F. Zhuo, D.-M. Lee, C. Sun, D. Seol, D. Lee, S.-W. Kim, Y. Kim, Mixed triboelectric and flexoelectric charge transfer at the nanoscale, *Advanced Science* 8 (20) (2021) 2101793. doi:10.1002/advs.202101793.
- [34] K. P. Olson, L. D. Marks, Is triboelectricity confusing, confused, or complex?, *Reports on Progress in Physics* 88 (10) (2025) 104501. doi:10.1088/1361-6633/ae08cb.
- [35] X. Xia, H. Wang, H. Guo, C. Xu, Y. Zi, On the material-dependent charge transfer mechanism of the contact electrification, *Nano Energy* 78 (2020) 105343. doi:10.1016/j.nanoen.2020.105343.
- [36] J. Lowell, Tunnelling between metals and insulators and its role in contact electrification, *Journal of Physics D: Applied Physics* 12 (9) (1979) 1541–1554. doi:10.1088/0022-3727/12/9/016.
- [37] W. R. Harper, Contact electrification of semiconductors, *British Journal of Applied Physics* 11 (8) (1960) 324–327. doi:10.1088/0508-3443/11/8/304.
- [38] F. A. Vick, Theory of contact electrification, *British Journal of Applied Physics* 4 (Supplement 2) (1953) S1–S5. doi:10.1088/0508-3443/4/S2/301.
- [39] A. M. Cowley, S. M. Sze, Surface states and barrier height of metal-semiconductor systems, *Journal of Applied Physics* 36 (10) (1965) 3212–3220. doi:10.1063/1.1702952.
- [40] S. Lin, C. Xu, L. Xu, Z. L. Wang, The overlapped electron-cloud model for electron transfer in contact electrification, *Advanced Functional Materials* 30 (11) (2020) 1909724. doi:10.1002/adfm.201909724.

- [41] C. Xu, Y. Zi, A. C. Wang, H. Zou, Y. Dai, X. He, P. Wang, Y.-C. Wang, P. Feng, D. Li, et al., On the electron-transfer mechanism in the contact-electrification effect, *Advanced materials* 30 (15) (2018) 1706790. doi:10.1002/adma.201706790.
- [42] A. F. Diaz, D. Fenzel-Alexander, An ion transfer model for contact charging, *Langmuir* 9 (4) (1993) 1009–1015. doi:10.1021/la00028a021.
- [43] C. Liu, A. J. Bard, Electrostatic electrochemistry at insulators, *Nature Materials* 7 (6) (2008) 505–509. doi:10.1038/nmat2160.
- [44] X. Ma, J. Zhou, E. Kim, J. Gao, W. Hu, D.-M. Shin, Quantifying electron and ion transfers in contact electrification with ionomers, *Advanced Functional Materials* (2025) 2506471doi:10.1002/adfm.202506471.
- [45] S. Pence, V. J. Novotny, A. F. Diaz, Effect of surface moisture on contact charge of polymers containing ions, *Langmuir* 10 (2) (1994) 592–596. doi:10.1021/la00014a042.
- [46] L. S. McCarty, G. M. Whitesides, Electrostatic charging due to separation of ions at interfaces: Contact electrification of ionic electrets, *Angewandte Chemie International Edition* 47 (12) (2008) 2188–2207. doi:10.1002/anie.200701812.
- [47] W. R. Salaneck, A. Paton, D. T. Clark, Double mass transfer during polymer-polymer contacts, *Journal of Applied Physics* 47 (1) (1976) 144–147. doi:10.1063/1.322306.
- [48] H. T. Baytekin, B. Baytekin, J. T. Incorvati, B. A. Grzybowski, Material transfer and polarity reversal in contact charging, *Angewandte Chemie International Edition* 51 (20) (2012) 4843–4847. doi:10.1002/anie.201200057.
- [49] R. K. Pandey, H. Kakehashi, H. Nakanishi, S. Soh, Correlating material transfer and charge transfer in contact electrification, *The Journal of Physical Chemistry C* 122 (28) (2018) 16154–16160. doi:10.1021/acs.jpcc.8b04357.
- [50] K. P. Olson, L. D. Marks, A quantitative model of triboelectric charge transfer, *Friction* 13 (2) (2025) 9440937. doi:10.26599/FRICT.2025.9440937.

- [51] D. Tan, Y. Zhang, Y. Liu, L. Chen, N. Wang, Z. Cai, W. Tang, H. Liu, Z. L. Wang, Electron transfer in the contact-electrification between corrugated 2D materials: A first-principles study, *Nano Energy* 79 (2021) 105386. doi:10.1016/j.nanoen.2020.105386.
- [52] C. Xu, B. Zhang, A. C. Wang, H. Zou, G. Liu, W. Ding, C. Wu, M. Ma, P. Feng, Z. Lin, Z. L. Wang, Contact-electrification between two identical materials: Curvature effect, *ACS Nano* 13 (2) (2019) 2034–2041. doi:10.1021/acsnano.8b08533.
- [53] M. Sow, R. Widenor, A. Kumar, S. W. Lee, D. J. Lacks, R. M. Sankaran, Strain-induced reversal of charge transfer in contact electrification, *Angewandte Chemie International Edition* 51 (11) (2012) 2695–2698. doi:10.1002/anie.201107256.
- [54] P. Zubko, G. Catalan, A. K. Tagantsev, Flexoelectric effect in solids, *Annual Review of Materials Research* 43 (1) (2013) 387–421. doi:10.1146/annurev-matsci-071312-121634.
- [55] B. Wang, Y. Gu, S. Zhang, L.-Q. Chen, Flexoelectricity in solids: Progress, challenges, and perspectives, *Progress in Materials Science* 106 (2019) 100570. doi:10.1016/j.pmatsci.2019.05.003.
- [56] W. Ma, L. E. Cross, Large flexoelectric polarization in ceramic lead magnesium niobate, *Applied Physics Letters* 79 (26) (2001) 4420–4422. doi:10.1063/1.1426690.
- [57] L. Shu, X. Wei, T. Pang, X. Yao, C. Wang, Symmetry of flexoelectric coefficients in crystalline medium, *Journal of Applied Physics* 110 (10) (2011) 104106. doi:10.1063/1.3662196.
- [58] T. D. Nguyen, S. Mao, Y.-W. Yeh, P. K. Purohit, M. C. McAlpine, Nanoscale flexoelectricity, *Advanced Materials* 25 (7) (2013) 946–974. doi:10.1002/adma.201203852.
- [59] K. M. Forward, D. J. Lacks, R. M. Sankaran, Charge segregation depends on particle size in triboelectrically charged granular materials, *Physical Review Letters* 102 (2) (2009) 028001. doi:10.1103/PhysRevLett.102.028001.
- [60] M. A. Bilici, J. R. Toth, R. M. Sankaran, D. J. Lacks, Particle size effects in particle-particle triboelectric charging studied with an integrated fluidized bed and electrostatic

- separator system, *Review of Scientific Instruments* 85 (10) (2014) 103903. doi:10.1063/1.4897182.
- [61] L. D. Marks, K. P. Olson, Flexoelectricity, triboelectricity, and free interfacial charges, *Small* 21 (28) (2025) 2310546. doi:10.1002/smll.202310546.
- [62] S. Mao, P. K. Purohit, Insights into flexoelectric solids from strain-gradient elasticity, *Journal of Applied Mechanics* 81 (8) (2014) 081004. doi:10.1115/1.4027451.
- [63] P. V. Yudin, A. K. Tagantsev, Fundamentals of flexoelectricity in solids, *Nanotechnology* 24 (43) (2013) 432001. doi:10.1088/0957-4484/24/43/432001.
- [64] X. Zhuang, B. H. Nguyen, S. S. Nanthakumar, T. Q. Tran, N. Alajlan, T. Rabczuk, Computational modeling of flexoelectricity—A review, *Energies* 13 (6) (2020) 1326. doi:10.3390/en13061326.
- [65] S. Mao, P. K. Purohit, N. Aravas, Mixed finite-element formulations in piezoelectricity and flexoelectricity, *Proceedings of the Royal Society A: Mathematical, Physical and Engineering Sciences* 472 (2190) (2016) 20150879. doi:10.1098/rspa.2015.0879.
- [66] F. Deng, Q. Deng, W. Yu, S. Shen, Mixed finite elements for flexoelectric solids, *Journal of Applied Mechanics* 84 (8) (2017) 081004. doi:10.1115/1.4036939.
- [67] A. Abdollahi, C. Peco, D. Millan, M. Arroyo, I. Arias, Computational evaluation of the flexoelectric effect in dielectric solids, *Journal of Applied Physics* 116 (9) (2014) 093502. doi:10.1063/1.4893974.
- [68] A. Abdollahi, D. Millán, C. Peco, M. Arroyo, I. Arias, Revisiting pyramid compression to quantify flexoelectricity: A three-dimensional simulation study, *Physical Review B* 91 (10) (2015) 104103. doi:10.1103/PhysRevB.91.104103.
- [69] T. J. R. Hughes, J. A. Cottrell, Y. Bazilevs, Isogeometric analysis: CAD, finite elements, nurbs, exact geometry and mesh refinement, *Computer Methods in Applied Mechanics and Engineering* 194 (39-41) (2005) 4135–4195. doi:10.1016/j.cma.2004.10.008.

- [70] V. P. Nguyen, C. Anitescu, S. P. Bordas, T. Rabczuk, Isogeometric analysis: an overview and computer implementation aspects, *Mathematics and Computers in Simulation* 117 (2015) 89–116. doi:10.1016/j.matcom.2015.05.008.
- [71] S. S. Nanthakumar, X. Zhuang, H. S. Park, T. Rabczuk, Topology optimization of flexoelectric structures, *Journal of the Mechanics and Physics of Solids* 105 (2017) 217–234. doi:10.1016/j.jmps.2017.05.010.
- [72] H. Ghasemi, H. S. Park, T. Rabczuk, A level-set based iga formulation for topology optimization of flexoelectric materials, *Computer Methods in Applied Mechanics and Engineering* 313 (2017) 239–258. doi:10.1016/j.cma.2016.09.029.
- [73] J. Yvonnet, L. P. Liu, A numerical framework for modeling flexoelectricity and maxwell stress in soft dielectrics at finite strains, *Computer Methods in Applied Mechanics and Engineering* 313 (2017) 450–482. doi:10.1016/j.cma.2016.09.007.
- [74] B. H. Nguyen, X. Zhuang, T. Rabczuk, NURBS-based formulation for nonlinear electro-gradient elasticity in semiconductors, *Computer Methods in Applied Mechanics and Engineering* 346 (2019) 1074–1095. doi:10.1016/j.cma.2018.08.026.
- [75] D. Codony, A. Mocci, J. Barceló-Mercader, I. Arias, Mathematical and computational modeling of flexoelectricity, *Journal of Applied Physics* 130 (23) (2021) 231102. doi:10.1063/5.0067852.
- [76] X. Zhuang, H. Hu, S. S. Nanthakumar, Q.-T. Tran, Y. Gong, T. Rabczuk, Variationally consistent maxwell stress in flexoelectric structures under finite deformation and immersed in free space, *Applied Mathematical Modelling* 150 (2025) 116327. doi:10.1016/j.apm.2025.116327.
- [77] H. Hu, Z. Liu, Q. Liu, X. Jiang, X. Zhuang, T. Rabczuk, Computational flexoelectronics: A framework for analyzing pn junctions in flexoelectric semiconductors, *International Journal of Mechanical Sciences* (2025) 110740doi:10.1016/j.ijmecsci.2025.110740.
- [78] U. Silavnieks, Q. Jing, N. Gadegaard, D. M. Mulvihill, Y. Xu, Flexoelectricity driven elastic contact-separation model for triboelectrification, *Friction* 13 (2025) 9441115. doi:10.26599/FRICT.2025.9441115.

- [79] D. Codony, P. Gupta, O. Marco, I. Arias, Modeling flexoelectricity in soft dielectrics at finite deformation, *Journal of the Mechanics and Physics of Solids* 146 (2021) 104182. doi:10.1016/j.jmps.2020.104182.
- [80] X.-P. Xu, A. Needleman, Void nucleation by inclusion debonding in a crystal matrix, *Modelling and Simulation in Materials Science and Engineering* 1 (2) (1993) 111–132. doi:10.1088/0965-0393/1/2/001.
- [81] M. J. Van den Bosch, P. J. G. Schreurs, M. G. D. Geers, An improved description of the exponential xu and needleman cohesive zone law for mixed-mode decohesion, *Engineering Fracture Mechanics* 73 (9) (2006) 1220–1234. doi:10.1016/j.engfracmech.2005.12.006.
- [82] R. Dimitri, M. Trullo, L. De Lorenzis, G. Zavarise, Coupled cohesive zone models for mixed-mode fracture: A comparative study, *Engineering Fracture Mechanics* 148 (2015) 145–179. doi:10.1016/j.engfracmech.2015.09.029.
- [83] M. Willatzen, Z. L. Wang, Contact electrification by quantum-mechanical tunneling, *Research* (2019) 6528689doi:10.34133/2019/6528689.
- [84] J. G. Simmons, Generalized formula for the electric tunnel effect between similar electrodes separated by a thin insulating film, *Journal of Applied Physics* 34 (6) (1963) 1793–1803. doi:10.1063/1.1702682.
- [85] P. Wriggers, *Computational Contact Mechanics*, 2nd Edition, Springer, Berlin, Heidelberg, 2006. doi:10.1007/978-3-540-32609-0.
- [86] J. Lu, X. Liang, W. Yu, S. Hu, S. Shen, Temperature dependence of flexoelectric coefficient for bulk polymer polyvinylidene fluoride, *Journal of Physics D: Applied Physics* 52 (7) (2019) 075302. doi:10.1088/1361-6463/aaf543.
- [87] Q. Deng, L. Liu, P. Sharma, Flexoelectricity in soft materials and biological membranes, *Journal of the Mechanics and Physics of Solids* 62 (2014) 209–227. doi:10.1016/j.jmps.2013.09.021.

- [88] C. Ishiyama, Y. Higo, Effects of humidity on young's modulus in poly(methyl methacrylate), *Journal of Polymer Science Part B: Polymer Physics* 40 (5) (2002) 460–465. doi:10.1002/polb.10107.
- [89] C. A. Harper, *Modern plastics handbook*, McGraw Hill Professional, 2000.
- [90] E. Tang, B. Leng, Y. Han, M. Xu, C. Chen, M. Chang, K. Guo, L. He, Mechanoelectric coupling model of polymethyl methacrylate under impact load, *Waves in Random and Complex Media* 35 (7) (2022) 13185–13207. doi:10.1080/17455030.2022.2139427.
- [91] Q. Guo, *Thermosets: structure, properties, and applications*, Woodhead Publishing, 2017. doi:10.1016/C2015-0-06205-0.
- [92] W. Jamieson, The electrification of insulating materials, *Nature* 83 (2113) (1910) 189. doi:10.1038/083189a0.
- [93] J. Lowell, W. S. Truscott, Triboelectrification of identical insulators. I. an experimental investigation, *Journal of Physics D: Applied Physics* 19 (7) (1986) 1273–1280. doi:10.1088/0022-3727/19/7/017.
- [94] M. M. Apodaca, P. J. Wesson, K. J. M. Bishop, M. A. Ratner, B. A. Grzybowski, Contact electrification between identical materials, *Angewandte Chemie International Edition* 49 (5) (2010) 946–949. doi:10.1002/anie.200905281.
- [95] H. T. Baytekin, A. Z. Patashinski, M. Branicki, B. Baytekin, S. Soh, B. A. Grzybowski, The mosaic of surface charge in contact electrification, *Science* 333 (6040) (2011) 308–312. doi:10.1126/science.1201512.
- [96] H. Hu, A. Batou, H. Ouyang, An isogeometric analysis based method for frictional elastic contact problems with randomly rough surfaces, *Computer Methods in Applied Mechanics and Engineering* 394 (2022) 114865. doi:10.1016/j.cma.2022.114865.